Paleoceanography and Paleoclimatology

RESEARCH ARTICLE
10.1029/2024PA004869

Key Points:

- We study the $^{231}Pa/^{230}Th$ proxy for Atlantic Meridional Overturning Circulation (AMOC) strength by comparing Bern3D model results to seawater observations and Holocene sediments
- Besides the Bermuda Rise, regions sensitive in $^{231}Pa/^{230}Th$ to AMOC changes are the equatorial West Atlantic and the northern North Atlantic
- An AMOC weakening largely reduces particles in the northern North Atlantic, causing a positive correlation between $^{231}Pa/^{230}Th$ and AMOC here

Supporting Information:

Supporting Information may be found in the online version of this article.

Correspondence to:

J. Scheen,
jeemijn.scheen@nioz.nl

Citation:

Scheen, J., Lippold, J., Pöppelmeier, F., Süfke, F., & Stocker, T. F. (2025). Promising regions for detecting the overturning circulation in Atlantic $^{231}Pa/^{230}Th$: A model-data comparison. *Paleoceanography and Paleoclimatology*, *40*, e2024PA004869. https://doi.org/10.1029/2024PA004869

Received 11 FEB 2024
Accepted 8 JAN 2025

Author Contributions:

Conceptualization: Jeemijn Scheen, Jörg Lippold, Frerk Pöppelmeier, Thomas F. Stocker
Data curation: Jeemijn Scheen, Jörg Lippold, Finn Süfke
Formal analysis: Jeemijn Scheen, Jörg Lippold, Frerk Pöppelmeier, Finn Süfke
Funding acquisition: Thomas F. Stocker
Investigation: Jeemijn Scheen, Jörg Lippold, Finn Süfke
Methodology: Jeemijn Scheen, Jörg Lippold, Frerk Pöppelmeier, Finn Süfke, Thomas F. Stocker
Project administration: Thomas F. Stocker
Resources: Jörg Lippold, Finn Süfke

Promising Regions for Detecting the Overturning Circulation in Atlantic $^{231}Pa/^{230}Th$: A Model-Data Comparison

Jeemijn Scheen[1,2,3], Jörg Lippold[4], Frerk Pöppelmeier[1,2], Finn Süfke[4], and Thomas F. Stocker[1,2]

[1]Climate and Environmental Physics, Physics Institute, University of Bern, Bern, Switzerland, [2]Oeschger Centre for Climate Change Research, University of Bern, Bern, Switzerland, [3]Department of Estuarine and Delta Systems, NIOZ Royal Netherlands Institute for Sea Research, Yerseke, The Netherlands, [4]Institute of Earth Sciences, Heidelberg University, Heidelberg, Germany

Abstract The Atlantic Meridional Overturning Circulation (AMOC) is a critical component of the climate system, strongly influencing the climate via ocean heat transport. The AMOC is thought to have had different characteristics during glacial periods and is expected to change under anthropogenic climate forcing. To reconstruct past AMOC strength, the $^{231}Pa/^{230}Th$ (protactinium-231 to thorium-230) ratio measured in marine sediments serves as an often used proxy. However, this ratio reflects not only circulation changes, but also effects from biological particle export and benthic nepheloid layers. Therefore, it remains an open question which regions exhibit a reliable AMOC signal in their sedimentary $^{231}Pa/^{230}Th$. We utilize the Bern3D model and a compilation of sediment $^{231}Pa/^{230}Th$ records, including records from 11 new core locations. This study suggests that equatorial West Atlantic $^{231}Pa/^{230}Th$ is as suitable as the Bermuda Rise region to detect AMOC changes. The $^{231}Pa/^{230}Th$ response to AMOC changes observed in part of the northern North Atlantic (which is opposite to regions further south) is caused mainly by AMOC-induced changes in particle production. Cores in this region are promising to reconstruct AMOC strength, despite exhibiting an AMOC-to-$^{231}Pa/^{230}Th$ relationship opposite from usual and high opal levels. Additional cores in the North Atlantic at 40°–60°N between 1 and 2 km depth are desirable for the application of $^{231}Pa/^{230}Th$. Our results suggest a new focus of $^{231}Pa/^{230}Th$ reconstructions on the equatorial West Atlantic and the northern North Atlantic, which appear to be best suited to quantify past AMOC strength.

1. Introduction

The strength of the Atlantic Meridional Overturning Circulation (AMOC) affects the climate in both hemispheres via ocean heat transport. There is an increasing body of evidence indicating that the AMOC experienced rapid variations in the past, for instance during the last deglaciation (Gebbie, 2014; Lynch-Stieglitz, 2017; Pöppelmeier et al., 2021; Repschläger et al., 2021). To reconstruct past AMOC strength, the ratio of protactinium-231 to thorium-230 measured in deep sea sediments is frequently used (Bradtmiller et al., 2014; Lippold, Luo, et al., 2012; McManus et al., 2004; Ng et al., 2018; Yu et al., 1996). Since the first reconstructions, the $^{231}Pa/^{230}Th$ records from Bermuda Rise sediments in the Northwest Atlantic are often considered as the standard records of past AMOC strength over the last 20,000 years, with high sediment $^{231}Pa/^{230}Th$ indicative of reduced AMOC strength, and vice versa (Böhm et al., 2015; Henry et al., 2016; Lippold et al., 2019; McManus et al., 2004). There are, however, still open questions on biases, as sediment $^{231}Pa/^{230}Th$ can be impacted by variable particle fluxes and bottom scavenging, with the latter being strongly present in the Bermuda Rise region (Gardner, Richardson, & Mishonov, 2018; Lerner et al., 2020). In addition, certain regions in the North Atlantic are assumed to show a positive correlation between sediment $^{231}Pa/^{230}Th$ and AMOC strength in the interpretation (Gherardi et al., 2009; Süfke et al., 2020), instead of the negative correlation as expected from simple geochemical considerations (Yu et al., 1996). In summary, interpreting Bermuda Rise $^{231}Pa/^{230}Th$ as a pure AMOC signal remains debated, while interpreting $^{231}Pa/^{230}Th$ records from other regions appears to be even more challenging.

^{231}Pa and ^{230}Th are both decay products of dissolved uranium, which is well-mixed in the ocean, such that the production rate of both isotopes is approximately uniform at a ^{231}Pa to ^{230}Th ratio of 0.093 (J. H. Chen et al., 1986). In contrast to uranium, dissolved ^{231}Pa and ^{230}Th are both highly particle reactive, with ^{231}Pa generally binding less well to particles than ^{230}Th (Anderson et al., 1983; Chase et al., 2002; S. Luo & Ku, 1999).

Software: Jeemijn Scheen, Frerk Pöppelmeier
Supervision: Jörg Lippold, Thomas F. Stocker
Visualization: Jeemijn Scheen
Writing – original draft: Jeemijn Scheen, Jörg Lippold
Writing – review & editing: Jeemijn Scheen, Jörg Lippold, Frerk Pöppelmeier, Thomas F. Stocker

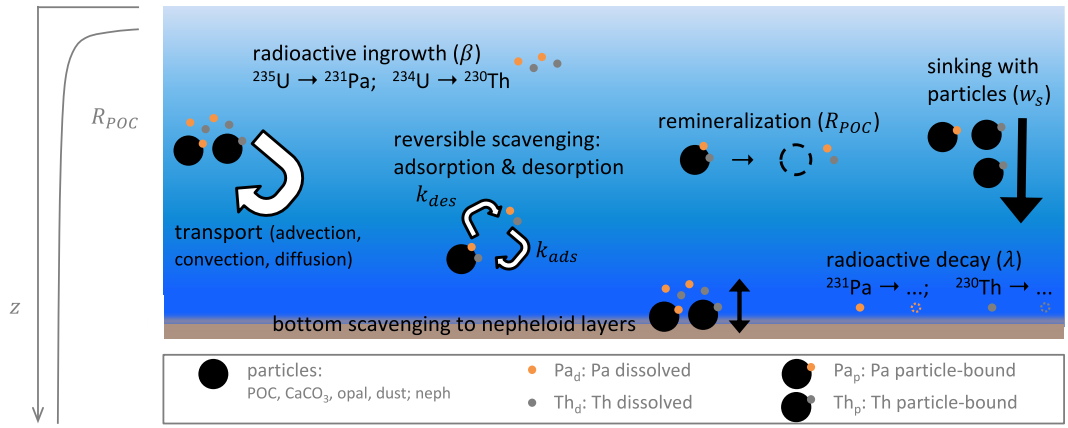

Figure 1. Schematic remineralization profile function $R_{POC}(z)$ (left) and processes of the protactinium and thorium cycle (right). Black circles in the ocean interior represent biogenic particles (POC, $CaCO_3$, opal) and dust, whereas black circles at the bottom are nepheloid-layer particles. Each process is simulated in the Bern3D model and has a corresponding term in Equations 5 and 6. Symbols are listed in Table 1.

In their particle-bound (particulate) form, ^{231}Pa and ^{230}Th sink along with the particles to the sediment (Figure 1). Dissolved ^{231}Pa has in general a longer residence time than ^{230}Th such that it can be more efficiently transported away from its production site. For instance, in the North Atlantic ^{231}Pa is advected southwards along with North Atlantic Deep Water (NADW) if the AMOC is strong. So if the AMOC strength increases, more dissolved ^{231}Pa is transported away out of the North Atlantic, and a sediment core in the North Atlantic will record a larger deficit in ^{231}Pa and hence a lower ^{231}Pa/^{230}Th ratio. This explains the classical anti-correlation between ^{231}Pa/^{230}Th and AMOC strength, which has been assumed in the studies on this proxy at the Bermuda Rise. The main sink of ^{231}Pa and ^{230}Th is adsorption onto biogenic or lithogenic particles sinking down the water column toward the sediment (Anderson et al., 1983). The adsorption (or "scavenging") onto particles is reversible (Bacon & Anderson, 1982): a continuous exchange occurs from dissolved to particle-bound forms (adsorption onto particles) and vice versa (desorption from particle surfaces). This chemical equilibrium would establish on a time scale of a few months (Bacon & Anderson, 1982; Henderson et al., 1999), but is continuously disturbed by other processes (see Figure 1). Different particle types have different scavenging behavior for ^{231}Pa and ^{230}Th. This poses a challenge for interpreting ^{231}Pa/^{230}Th since particle types vary between regions and over time. Other particle types have been observed to play a role in the cycling of ^{231}Pa and ^{230}Th as well, such as particles from riverine input and hydrothermal vents (Fe-Mn oxyhydroxides) (Hayes, Anderson, Fleisher, Vivancos, et al., 2015). Further sinks are scavenging by nepheloid-layer particles close to the seafloor, also called bottom scavenging (Deng et al., 2014; Okubo et al., 2012), and radioactive decay with half-lives of 32.8 kyr (^{231}Pa) and 75.6 kyr (^{230}Th), which are negligible compared to the other sinks in the modern ocean. Finally, particle-bound ^{231}Pa and ^{230}Th also transform back to their dissolved forms when particles remineralize at depth.

Simulating the cycles of ^{231}Pa and ^{230}Th in the oceans received increasing attention in the last decade (S.-Y. S. Chen et al., 2021; Gu & Liu, 2017; Gu et al., 2020; Lerner et al., 2020; Y. Luo et al., 2021; Missiaen, Bouttes, et al., 2020, Missiaen, Menviel, et al., 2020; Rempfer et al., 2017; Sasaki et al., 2022; van Hulten et al., 2018), with ^{231}Pa and ^{230}Th tracers now implemented in a number of ocean models. Early one-dimensional (vertical) models already established a firm understanding of reversible scavenging of Th isotopes (Bacon & Anderson, 1982), which was later implemented for ^{231}Pa and ^{230}Th in a latitude-depth transport model (Y. Luo et al., 2010), in a zonally-averaged multi-basin circulation-biogeochemistry model (Marchal et al., 2000), in 3D inverse models (Burke et al., 2011; Marchal et al., 2007) and in 3D ocean circulation-biogeochemistry models (Dutay et al., 2009; Gu & Liu, 2017; Henderson et al., 1999; Lerner et al., 2020; Missiaen, Bouttes, et al., 2020; Rempfer et al., 2017; Sasaki et al., 2022; Siddall et al., 2005). For 3D models with a dynamically simulated ocean, two main implementations to simulate ^{231}Pa and ^{230}Th exist. We refer to these here as the "diagnostic" and the "prognostic" approach, based on the nature of their governing equations for ^{231}Pa and ^{230}Th (Appendix A). Briefly, the diagnostic approach assumes instantaneous equilibrium between dissolved and particle-bound phases, whereas

the prognostic approach allows for an evolution toward adsorption-desorption equilibria over time and a possible influence by other processes.

Many of these previous modeling studies investigated the response of a weakened AMOC on sedimentary $^{231}Pa/^{230}Th$. These studies consistently found that the $^{231}Pa/^{230}Th$ ratio increases in most of the North Atlantic and decreases in the South Atlantic, as the southwards transport of ^{231}Pa is curtailed during weaker AMOC states (e.g., Gu & Liu, 2017; Marchal et al., 2000; Missiaen, Bouttes, et al., 2020; Rempfer et al., 2017). The scavenging parameters in models were tuned to observations by Marchal et al. (2000), Rempfer et al. (2017), and Missiaen, Bouttes, et al. (2020), but they found no consensual values due to differences in approach, observational data sets and between models. Some studies investigated which particle types are most important for $^{231}Pa/^{230}Th$ and they found a key role for opal (e.g., Missiaen, Menviel, et al., 2020; Siddall et al., 2005). Moreover, the studies by Rempfer et al. (2017), Lerner et al. (2020), and Sasaki et al. (2022) highlighted the importance of incorporating bottom scavenging to achieve a good representation of the modern distributions of dissolved ^{231}Pa and ^{230}Th.

In this study, we employ a state-of-the-art $^{231}Pa/^{230}Th$ implementation in the Bern3D model, which we have tuned to match modern observations (Deng et al., 2018; GEOTRACES Intermediate Data Product Group, 2021; Ng et al., 2020; Pavia et al., 2020). We have added spatially resolved nepheloid layers to the model, which are important for bottom scavenging. As the first study, we deliberately added bottom scavenging before tuning particle scavenging coefficients. In a number of experiments, we explore the impact of varying AMOC, particle fluxes or both simultaneously. This enables us to estimate sensitivities of regional $^{231}Pa/^{230}Th$ to changes in AMOC strength. Comparisons to water column and sedimentary $^{231}Pa/^{230}Th$ measurements help to build confidence in the model, and allow us to identify why certain regions carry a $^{231}Pa/^{230}Th$ signal that correlates positively with AMOC strength while others are characterized by a negative correlation.

2. Methods

2.1. The Bern3D Model

We employ the Bern3D Earth system Model of Intermediate Complexity, version 2.0, which has an ocean grid resolution of 41 × 40 in longitude by latitude, 32 ocean depth layers and a time step of 3.8 days (Roth et al. (2014), Appendix). The model contains coupled components for the ocean, land, and atmosphere, which exchange fluxes of heat, carbon, and freshwater via evaporation, precipitation and runoff. The ocean is dynamically simulated based on frictional geostrophic balance equations (Edwards et al., 1998; Müller et al., 2006). A monthly wind climatology (Kalnay et al., 1996) applies wind stress to the surface ocean, whereas sea-ice growth, melt and advection are simulated. The simplified atmosphere consists of a single-layer energy-moisture balance model (Ritz et al., 2011) with a prescribed albedo distribution. Export production is simulated for particulate organic carbon (POC), calcium carbonate ($CaCO_3$) and biogenic opal in the surface ocean (Parekh et al., 2008) based on light, nutrient limitation (phosphate, silicate, iron) and temperature, which results in the steady state export fluxes as shown in Figures 2a–2c under pre-industrial conditions (annual average). The implementation of $CaCO_3$ in the model is simplified and based on a fixed rain ratio. Simulated $CaCO_3$ export equals simulated POC export scaled by a factor 0.075, except in regions with high silicic acid concentrations, where opal production is favored (Roth et al., 2014). Compared to observations (Sarmiento and Gruber (2006), color plate 4), the Bern3D model is able to reproduce the main features of particle export from 60°S to 60°N (Roth et al., 2014), albeit with certain shortcomings. The POC pattern agrees well with observations, but simulated export fluxes are consistently too high by around a factor 2 everywhere, except in the northern North Atlantic, where simulated POC export is too low. For $CaCO_3$, the gradient between the regions with low and high export is not large enough in the model; simulated $CaCO_3$ remains too high inside the subtropical gyres. Moreover, in the observations reported by Sarmiento and Gruber (2006) $CaCO_3$ is virtually absent south of 50°N. Simulated opal export corresponds very well with Sarmiento and Gruber (2006), except a too narrow Southern Ocean opal belt, which should extend southwards toward the Antarctic coast.

Particle fluxes $F_i(\theta, \phi, z)$ of particle type i remineralize instantaneously below the euphotic zone following the Martin-curve (Martin et al., 1987) for POC and exponential decays for $CaCO_3$ and biogenic opal (Rempfer et al., 2011):

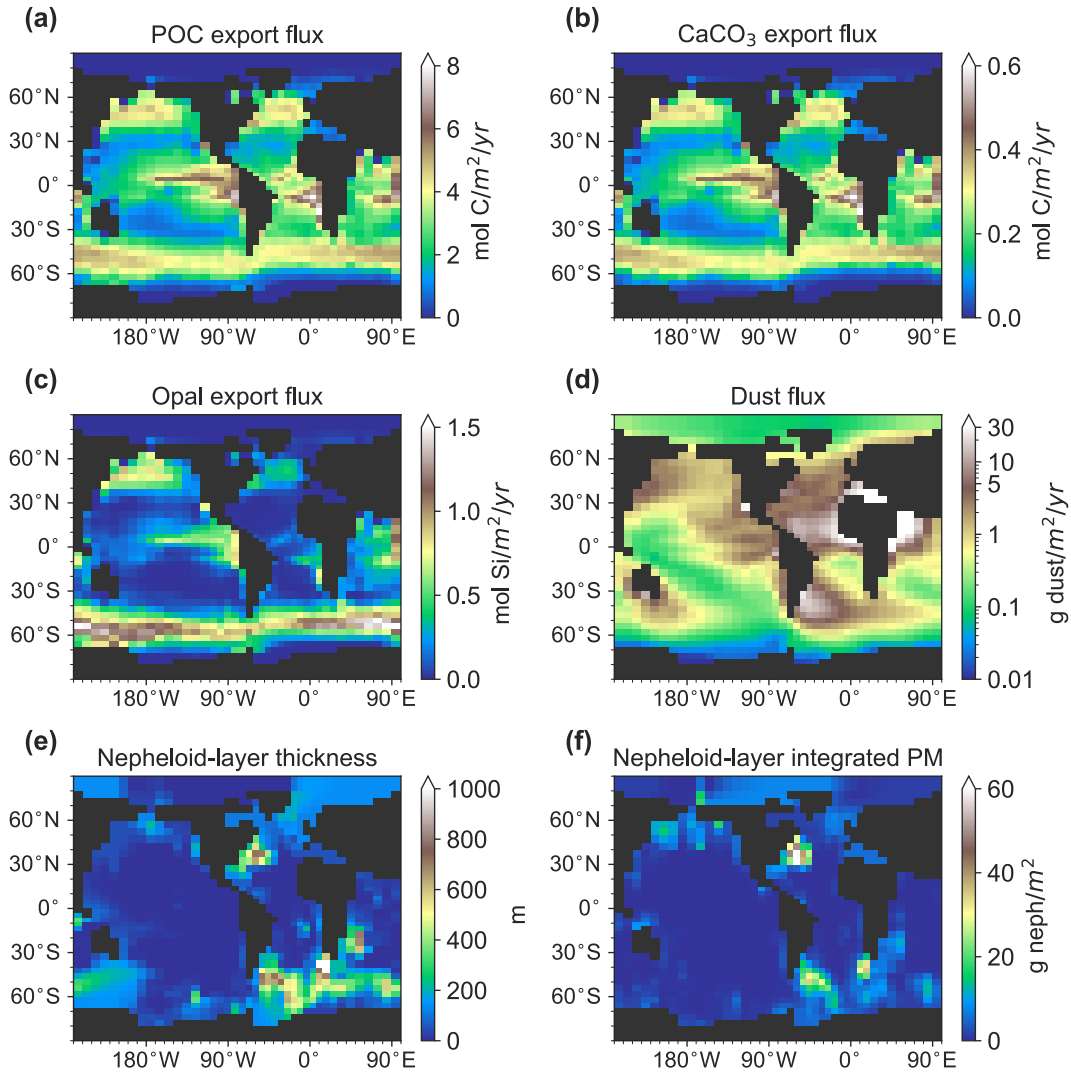

Figure 2. Particle export flux $F_i(\theta, \phi, z_{eu})$ at the bottom of the euphotic zone (75 m) as simulated by the Bern3D biogeochemical module at pre-industrial steady state for (a) particulate organic carbon, (b) calcium carbonate, and (c) opal. (d) Dust export flux $F_{du}(\theta, \phi, z)$ based on observations (Mahowald et al., 2006) on a logarithmic color scale. Mean annual export fluxes are shown, while in model simulations a seasonal cycle is present for panels (a)–(d). Note the different color scales and different units. (e) Nepheloid-layer thickness $H_{ne}(\theta, \phi)$ and (f) excess particulate matter (PM) load $m_{ne}^{tot}(\theta, \phi)$, based on Gardner, Richardson, Mishonov, et al. (2018).

$$F_i(\theta, \phi, z) = F_i(\theta, \phi, z_{eu}) \cdot R_i(z) \tag{1}$$

for $z > z_{eu} = 75$ m, where $F_i(\theta, \phi, z_{eu})$ is the export flux at the base of the euphotic zone, $z = z_{eu}$, and $R_i(z)$ is a remineralization function between 0 and 1:

$$R_{POC}(z) = \left(\frac{z}{z_{eu}}\right)^{-\alpha}, \tag{2}$$

$$R_{ca}(z) = \exp\left(-\frac{z - z_{eu}}{l_{ca}}\right), \tag{3}$$

$$R_{op}(z) = \exp\left(-\frac{z - z_{eu}}{l_{op}}\right). \tag{4}$$

Table 1
Parameters and Variables of the Protactinium-Thorium Module

Symbol	Definition	Value	Unit
i	Particle type index	POC, $CaCO_3$, opal, dust or neph	–
j	Nuclide index	^{231}Pa or ^{230}Th	–
$^{231}Pa_d$	Activity of dissolved ^{231}Pa	Simulated (Equation 5)	μBq/kg
$^{230}Th_d$	Activity of dissolved ^{230}Th	Simulated (Equation 5)	μBq/kg
$^{231}Pa_p$	Activity of particle-bound ^{231}Pa	Simulated (Equation 6)	μBq/kg
$^{230}Th_p$	Activity of particle-bound ^{230}Th	Simulated (Equation 6)	μBq/kg
β^{Pa}	Radioactive production of ^{231}Pa from U	$2.33 \cdot 10^{-3}$	dpm m^{-3} yr^{-1}
β^{Th}	Radioactive production of ^{230}Th from U	$2.52 \cdot 10^{-2}$	dpm m^{-3} yr^{-1}
λ^{Pa}	Radioactive decay constant of ^{231}Pa	$2.13 \cdot 10^{-5}$	yr^{-1}
λ^{Th}	Radioactive decay constant of ^{230}Th	$9.22 \cdot 10^{-6}$	yr^{-1}
w_s	Uniform sinking speed of particles	1,600	m/yr
k^j_{des}	Desorption rate constant	4.0	yr^{-1}
$k^j_{ads}(\theta,\phi,z)$	Adsorption rate constant	Equation 7	yr^{-1}
σ^j_i	Scavenging coefficients	Table 3	see Table 3
$R_i(z)$	Remineralization function	Equations 2–4	–
$F_i(\theta,\phi,z)$	Downward particle flux (for $i \neq neph$)	Equation 1; Figures 2a–2d	see Figures 2a–2d
$F_{ne}(\theta,\phi,z)$	Downward particle flux (for $i = neph$)	Equation 9	g neph m^{-2} yr^{-1}
$H_{ne}(\theta,\phi)$	Thickness of nepheloid layer	Figure 2e	m
$m^{tot}_{ne}(\theta,\phi)$	Mass of nepheloid-layer particles, integrated over layer	Figure 2f	g neph m^{-2}

with exponent $\alpha = 0.83$ (Roth et al., 2014) and length scales $l_{ca} = 5066$ m (Jeltsch-Thömmes et al., 2019) and $l_{op} = 10,000$ m (Tschumi et al., 2008).

2.2. Model Development of ^{231}Pa and ^{230}Th Tracers

We simulate ^{231}Pa and ^{230}Th with the prognostic approach, which is physically more realistic than the diagnostic approach. Variables and parameters are listed in Table 1. We report specific activities A (called concentrations in this study) in μBq kg^{-1} for easier comparability to seawater observations. Dissolved concentrations of ^{231}Pa and ^{230}Th are denoted throughout this study with the subscript d and particle-bound concentrations with subscript p. In equations, we abbreviate activities (concentrations) of dissolved forms as A^j_d with $j \in [^{231}\text{Pa}, ^{230}\text{Th}]$ and particle-bound forms as A^j_p. Compared to Rempfer et al. (2017), we added dust as another scavenging particle type, updated bottom scavenging due to nepheloid layers, performed a systematic tuning of the scavenging coefficients to new observations (Section 2.5) and removed explicit boundary scavenging. The governing equations in our simulations are as in Rempfer et al. (2017):

$$\frac{\partial A^j_d}{\partial t} = \text{Transport}\left(A^j_d\right) - \lambda^j A^j_d + k^j_{\text{des}} A^j_p - k^j_{\text{ads}} A^j_d + \beta^j, \tag{5}$$

$$\frac{\partial A^j_p}{\partial t} = \text{Transport}\left(A^j_p\right) - \lambda^j A^j_p - k^j_{\text{des}} A^j_p + k^j_{\text{ads}} A^j_d - w_s \frac{\partial A^j_p}{\partial z}. \tag{6}$$

The tracers are subject to oceanic transport (advection, convection and diffusion). Sources and sinks are: radioactive decay with radioactive constant λ^j, production by decay from a parent nuclide β^j and scavenging by particles sinking with speed w_s (last term of Equation 6). Scavenging is parameterized via adsorption and desorption rate constants:

$$k^j_{\text{ads}}(\theta,\phi,z) = \sum_i \sigma^j_i \cdot F_i(\theta,\phi,z), \tag{7}$$

$$k^j_{\text{des}} = 4.0\ \text{yr}^{-1}, \tag{8}$$

$$i \in [POC, CaCO_3, opal, dust, neph]$$
$$j \in [^{231}\text{Pa}, ^{230}\text{Th}]$$

where σ^j_i are globally uniform scavenging coefficients expressing how strongly particle type i adsorbs tracer j.

Lithogenic particles in the form of dust and nepheloid-layer particles are also considered in Equation 7. Dust fields are prescribed after the model output from Mahowald et al. (2006), whereas nepheloid-layer concentrations and thickness are derived from Gardner, Richardson, Mishonov, et al. (2018), inspired by Lerner et al. (2020). We assume no remineralization of dust and nepheloid-layer particles, because they dissolve little while sinking through the water column to the sediment (Carroll & Starkey, 1958). The spatial distribution of nepheloid layers is based on nephelometer and transmissometer data reported by Gardner, Richardson, Mishonov, et al. (2018). The authors provide thicknesses of nepheloid layers, H_{ne}, and excess particulate matter load (i.e., in excess relatively to biological particles and dust) integrated over the nepheloid-layer height, m^{tot}_{ne} in g m^{-2}. We combine these two quantities to find a flux $F_{ne}(\theta,\phi,z)$ (see paragraph below). We use for H_{ne} the transmissometer results (their Figure 2a), because they are derived from data with a better depth resolution, and for m^{tot}_{ne} we take the combination of transmissometer and nephelometer data (their Figure 3c), which is available in this case. These variables were regridded and data gaps were filled (see Text S1 in Supporting Information S1).

We distribute the vertically-integrated excess particulate matter load, $m^{tot}_{ne}(\theta,\phi)$, uniformly over the height of the nepheloid layer, $H_{ne}(\theta,\phi)$, yielding a nepheloid particulate matter concentration of $m^{tot}_{ne}(\theta,\phi)/H_{ne}(\theta,\phi)$ throughout the nepheloid-layer part of a water column. This simplification only has a small impact as the nepheloid layer consists of a maximum of three vertical grid cells in the open ocean (grid cells are particularly thick close to the bottom: up to 400 m at 5 km depth). Converting concentration to flux via the sinking speed w_s, which we take identical for all particle types, gives:

$$F_{ne}(\theta,\phi,z) = \frac{w_s \cdot m^{tot}_{ne}(\theta,\phi)}{H_{ne}(\theta,\phi)} \tag{9}$$

for z in the nepheloid layer ($F_{ne} = 0$ elsewhere). This $F_{ne}(\theta,\phi,z)$ is then used in Equation 7.

We also tested the effect of a benthic flux of ^{231}Pa and ^{230}Th coming out of the sediment. Opal particles remineralize slowly, and most opal that reaches the ocean floor is still dissolving within the sediment (Abrantes, 2000), from where opal can release opal-bound ^{231}Pa or ^{230}Th again into the pore water as dissolved ^{231}Pa or ^{230}Th. This could potentially affect the ^{231}Pa and ^{230}Th budgets in the deep ocean, and was so far not considered in models. We simulated 20% of the opal-bound ^{231}Pa and/or ^{230}Th as a source of dissolved ^{231}Pa or ^{230}Th at the bottom-most grid cells. However, this made no visible difference such that we decided not to include this process in the model.

2.3. Seawater Data

Seawater data from the GEOTRACES Intermediate Data Product Group (2021), from Deng et al. (2018), Ng et al. (2020), and Pavia et al. (2020) were used for model tuning. These consist of measurements of $^{231}\text{Pa}_\text{d}$, $^{230}\text{Th}_\text{d}$, $^{231}\text{Pa}_\text{p}$ and $^{230}\text{Th}_\text{p}$ taken from 2008 to 2020. We excluded the Arctic basin, as Arctic water masses cannot be realistically simulated with the coarse resolution of the Bern3D model.

We used all available measurements from Deng et al. (2018), Ng et al. (2020), and Pavia et al. (2020). The GEOTRACES Intermediate Data Product Group (2021) measurements were performed by Venchiarutti et al. (2011), Hayes et al. (2013), Deng et al. (2014), Hayes, Anderson, Fleisher, Huang, et al. (2015), Hayes, Anderson, Fleisher, Vivancos, et al. (2015), Anderson et al. (2016), Hayes et al. (2017), Roy-Barman et al. (2019), and Pavia et al. (2019). For dissolved ^{231}Pa and ^{230}Th, we only considered measurements from bottles (98% of all

measurements) and those labeled as "good quality" (98% of the bottle measurements). Three types of measured particulate ^{231}Pa and ^{230}Th data are available from the data product, all determined by in situ filtration (pump): without size fractionation, collected on a main filter (small particles) and collected on a pre filter (large particles). We used all these types together as $^{231}Pa_p$ and $^{230}Th_p$, using only those labeled good quality (99%).

In total, we used 1,646 $^{231}Pa_d$ (1,857 $^{230}Th_d$) seawater measurements from 122 (151) stations. For $^{231}Pa_p$ we used 548 (for $^{230}Th_p$ 648) seawater measurements from 50 (59) stations. Reported uncertainties were on average 6%, 4%, 11%, and 5% of measured values for $^{231}Pa_d$, $^{230}Th_d$, $^{231}Pa_p$ and $^{230}Th_p$, respectively. If multiple measurements fell in the same model grid cell, they were combined into a single value obs_l (used later in Equation 11) by averaging with weights $a_{i,l} = 1/e_{i,l}$ with $e_{i,l}$ the uncertainty of a single observation i in grid cell l. Measurement uncertainties were propagated as appropriate for weighted averages:

$$e_l = \frac{\sqrt{\sum_{i=1}^{M} (a_{i,l})^2 \cdot (e_{i,l})^2}}{\sum_{i=1}^{M} a_{i,l}}, \tag{10}$$

where M is the number of measurements in grid cell l. This collection of seawater data was used for model tuning (Section 2.5 and Text S3 in Supporting Information S1) and is partially shown in Figures C1 and 5; Figures S5–S7 in Supporting Information S1 as model-data comparison.

2.4. New and Published Sediment Data

For this study, we compiled Atlantic $^{231}Pa_p/^{230}Th_p$ records combining data from 93 published sediment cores and 11 new records (Figure 3a). The new cores improve the spatial coverage of the data set available from the literature, in particular filling gaps over a wide range of water depths in the South Atlantic. For this compilation, we chose the Atlantic basin, except its Southern Ocean sector, as domain in order to include cores potentially dominated by an AMOC signal. Cores from the Southern Ocean opal belt are highly correlated with very local particle fluxes, which cannot be simulated in sufficient horizontal resolution, such that the Atlantic sector of the Southern Ocean was excluded from our compilation of sediment $^{231}Pa_p/^{230}Th_p$ data.

For the new ^{231}Pa/^{230}Th records, sediment samples have been analyzed for the concentration of the radioisotopes ^{230}Th, ^{231}Pa, ^{232}Th, ^{234}U, and ^{238}U. Per sample approximately 0.1 g of sediment was weighed and then spiked with ^{233}Pa, ^{229}Th and ^{236}U prior to chemical treatment, followed by total digestion in a mixture of concentrated HCl, HNO_3 and HF. Purification and separation of ^{231}Pa, ^{230}Th and U followed the standard protocols described by Süfke et al. (2018). The short-lived ^{233}Pa spike ($t_{1/2}$ = 27 days) was milked from a ^{237}Np solution using the procedure described by Regelous et al. (2004). The ^{233}Pa spike was calibrated against an internal pitchblende standard (Fietzke et al., 1999) and the reference material IAEA-385 (Süfke et al., 2018). Isotope measurements were performed on a Neptune Plus MC-ICP-MS in the Geozentrum Nordbayern at Erlangen, Germany, and on an iCAP TQe ICP-MS at the Institute of Earth Sciences of Heidelberg University. ^{230}Th, ^{232}Th and ^{238}U generally had full-process blank contributions lower than 1%; ^{231}Pa below 2%. The desired excess fractions (i.e., the ^{231}Pa and ^{230}Th produced in the overlying water column from decay of dissolved uranium) were calculated from the measured total concentrations by correcting for detrital and authigenic input and radioactive decay since the time of deposition following the suggestions by Bourne et al. (2012) (see Text S2 in Supporting Information S1). Age models are also described in Text S2 in Supporting Information S1.

An overview of the observational ^{231}Pa/^{230}Th database used for this study is provided in Table 2, indicating the ^{231}Pa/^{230}Th average over the Holocene (defined here as the 0–8 ka time interval). Published Holocene data of ^{231}Pa/^{230}Th-records were used here from Anderson et al. (2014), Bradtmiller et al. (2007, 2014), Burckel et al. (2015), Gherardi et al. (2005, 2009), Hall et al. (2006), Hickey (2010), Hoffmann et al. (2018), Lippold et al. (2011, 2012a), Lippold, Mulitza, et al. (2012), Lippold et al. (2016), Lippold et al. (2019), McManus et al. (2004), Mulitza et al. (2017), Negre et al. (2010), Ng et al. (2018, 2020), Roberts et al. (2014), Süfke et al. (2019, 2020), and Waelbroeck et al. (2018). If multiple samples were available for one core, we averaged the measurements over the mid-to-late Holocene (0–8 ka). The standard error (SE) was computed as the standard deviation of the uncertainties of the n samples divided by $\sqrt{n}$. We considered Holocene data from 0 to 8 ka only in

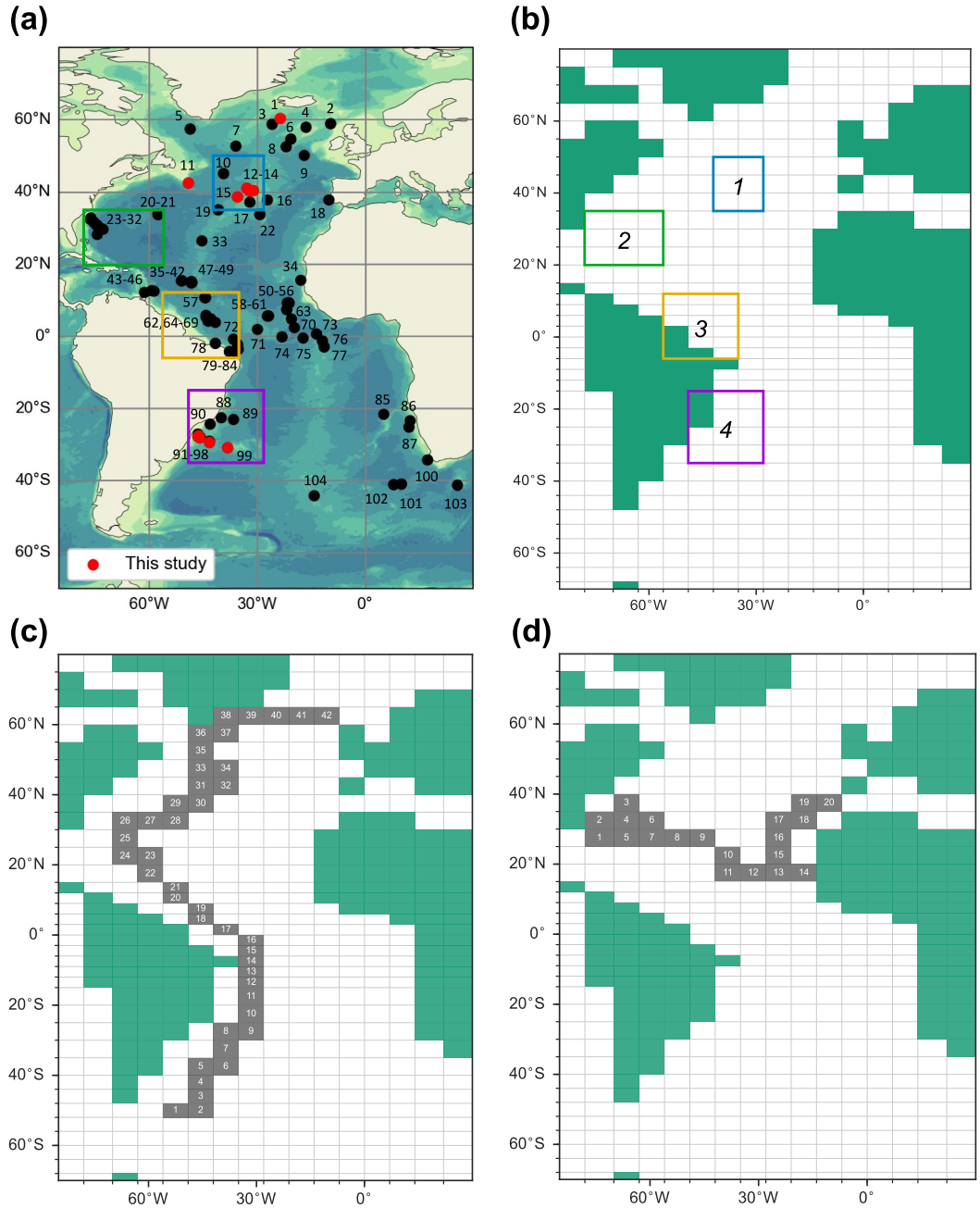

Figure 3. (a) Sediment cores used in this study. See also Table 2. Red circles indicate new $^{231}Pa/^{230}Th$ from this study. (b) Bern3D model grid in the Atlantic with the four regions of interest that are used in Figure 10. Boundaries are 35°–50°N, 42°–28°W for region 1 (northern North Atlantic); 20°–35°N, 78°–56°W for region 2 (Bermuda Rise); 6°S–12°N, 56°–35°W for region 3 (equatorial West Atlantic); and 35°–15°S, 49°–28°W for region 4 (Southwest Atlantic). (c) Trajectories of GEOTRACES transect GA02 and (d) GA03. Numbering of water columns corresponds to the lower *x*-axes in Figures 5 and 11.

order to avoid data that are influenced by the higher deglacial AMOC variability, assuming a relatively stable AMOC during the Holocene (Hoffmann et al., 2018; Lippold et al., 2019).

The Holocene sediment database was used to validate the tuned model results at the pre-industrial and to identify regions and water depths of high sensitivity of $^{231}Pa_p/^{230}Th_p$ to AMOC changes (Section 3.1).

Table 2
Sediment Measurements

Index number	Core	Lat	Lon	Depth	Holocene (0–8 ka) Pa/Th	*n*	SE	Reference	Region
1	ODP 983	60.40	−23.64	1,984	0.126	2	0.007	This study	
2	DACP2	58.97	−9.61	1,709	0.093	4	0.002	Hall et al. (2006)	
3	MD95-2015	58.76	−25.96	2,630	0.120	1	0.004	Lippold, Luo, et al. (2012)	
4	BOFS 17K	58.00	−16.50	1,150	0.123	6	0.010	Roberts et al. (2014)	
5	GS06-144-02GC	57.48	−48.62	3,440	0.110	1	0.003	Lippold, Luo, et al. (2012)	
6	BOFS 10K	54.70	−20.70	2,777	0.073	8	0.003	Roberts et al. (2014)	
7	MD08-3182CQ	52.70	−35.94	3,757	0.103	1	0.003	Lippold, Luo, et al. (2012)	
8	BOFS 8K	52.50	−22.06	4,045	0.068	2	0.005	Roberts et al. (2014)	
9	SU90-44	50.20	−17.00	4,279	0.051	5	0.005	Gherardi et al. (2009)	
10	SU90-I02	45.09	−39.44	1,965	0.091	9	0.023	Süfke et al. (2020)	1
11	GeoB18530-1	42.50	−49.14	1,888	0.088	4	0.006	This study	
12	IODP 1313	41.00	−32.96	3,413	0.053	6	0.001	This study	1
13	MSM58-13-2	40.40	−31.08	2,102	0.074	6	0.004	This study	1
14	SU90-03	40.31	−32.04	2,475	0.057	6	0.003	This study	1
15	MSM58-28-4	38.58	−35.54	4,110	0.050	3	0.001	This study	1
16	SU92-18	37.79	−27.23	2,300	0.071	1	0.006	Lippold, Luo, et al. (2012)	
17	MD95-2037	37.10	−32.00	2,159	0.094	7	0.007	Gherardi et al. (2009)	1
18	SU81-18	37.80	−10.20	3,135	0.064	9	0.008	Gherardi et al. (2005)	
19	V27-263	35.02	−40.92	3,704	0.037	1	0.001	Bradtmiller et al. (2007)	1
20	OCE326-GGC5	33.70	−57.60	4,550	0.055	8	0.003	McManus et al. (2004)	2
21	ODP 1063	33.69	−57.61	4,584	0.057	52	0.002	Lippold et al. (2019)	2
22	V29-172	33.70	−29.38	3,457	0.054	1	0.001	Bradtmiller et al. (2007)	
23	ODP 1055	32.78	−76.29	1,798	0.065	1	0.003	Lippold, Luo, et al. (2012)	2
24	KN140-2-51GGC	32.78	−76.28	1,790	0.069	19	0.004	Hoffmann et al. (2018)	2
25	ODP 1056	32.48	−76.33	2,166	0.059	1	0.002	Lippold, Luo, et al. (2012)	2
26	ODP 1058	31.69	−75.43	2,984	0.060	1	0.003	Lippold, Luo, et al. (2012)	2
27	ODP 1059	31.67	−75.42	2,985	0.060	7	0.008	Süfke et al. (2019)	2
28	KNR140 31GGC	30.90	−74.50	3,410	0.066	1	0.003	Bradtmiller et al. (2007)	2
29	ODP 1060	30.76	−74.57	3,481	0.056	5	0.003	Süfke et al. (2019)	2
30	ODP 1061	29.98	−73.60	4,038	0.056	5	0.002	Süfke et al. (2019)	2
31	12JPC	29.75	−72.90	4,250	0.060	3	0.001	Süfke et al. (2019)	2
32	ODP 1062	28.25	−74.41	4,761	0.052	4	0.001	Süfke et al. (2019)	2
33	V25-21	26.40	−45.45	3,693	0.046	1	0.001	Bradtmiller et al. (2007)	
34	GeoB9508-5	15.50	−17.95	2,384	0.109	3	0.010	Lippold, Luo, et al. (2012)	
35	Gramberg JC094-S0177_CT	15.46	−50.99	2,714	0.061	1	0.002	Ng et al. (2020)	
36	JC094-GVY14	15.46	−50.99	2,714	0.057	3	0.009	Ng et al. (2018)	
37	Gramberg JC094-S0170_CT	15.44	−51.10	1,675	0.095	1	0.003	Ng et al. (2020)	
38	Gramberg JC094-S0161_CT	15.42	−51.09	1,379	0.122	1	0.004	Ng et al. (2020)	
39	Vayda JC094-S0131_CT	15.17	−48.25	4,126	0.055	1	0.002	Ng et al. (2020)	
40	Vayda JC094-S0138_CT	14.89	−48.12	1,055	0.160	1	0.006	Ng et al. (2020)	

Table 2
Continued

Index number	Core	Lat	Lon	Depth	Holocene (0–8 ka) Pa/Th	*n*	SE	Reference	Region
41	Vayda JC094-S0140_CT	14.85	−48.27	2,166	0.074	1	0.002	Ng et al. (2020)	
42	Vayda JC094-S0157_CT	14.77	−48.25	3,721	0.060	1	0.002	Ng et al. (2020)	
43	GeoB3936-1	12.72	−59.00	1,854	0.078	1	0.003	Lippold et al. (2011)	
44	GeoB3935-2	12.61	−59.39	1,558	0.082	1	0.004	Lippold et al. (2011)	
45	GeoB3937-2	12.56	−58.77	1,654	0.079	1	0.003	Lippold et al. (2011)	
46	M35003	12.09	−61.24	1,300	0.109	2	0.003	Lippold et al. (2016)	
47	Vema JC094-S0120_CT	10.78	−44.60	2,932	0.071	1	0.003	Ng et al. (2020)	3
48	Vema JC094-S0114A_CT	10.73	−44.42	1,094	0.209	1	0.006	Ng et al. (2020)	3
49	Vema JC094-S0119_CT	10.71	−44.42	570	0.268	1	0.008	Ng et al. (2020)	3
50	Carter JC094-S0021_CT	9.28	−21.64	4,565	0.048	1	0.002	Ng et al. (2020)	
51	Carter JC094-S0058_CT	9.22	−21.31	684	0.228	1	0.007	Ng et al. (2020)	
52	Carter JC094-S0055_CT	9.21	−21.30	1,366	0.199	1	0.006	Ng et al. (2020)	
53	Carter JC094-S0036_CT	9.18	−21.27	2,719	0.082	1	0.003	Ng et al. (2020)	
54	Carter JC094-S0039_CT	9.17	−21.27	2,278	0.104	1	0.004	Ng et al. (2020)	
55	JC094-GVY01	7.44	−21.80	3,426	0.048	2	0.001	Ng et al. (2018)	
56	Carter JC094-S0066_CT	7.43	−21.80	3,419	0.071	1	0.004	Ng et al. (2020)	
57	EW9209 1JPC	5.91	−44.20	4,056	0.043	4	0.001	Ng et al. (2018)	3
58	Knipovich JC094-S0085_CT	5.71	−27.27	4,405	0.045	1	0.002	Ng et al. (2020)	
59	Knipovich JC094-S0074_CT	5.63	−26.96	990	0.193	1	0.006	Ng et al. (2020)	
60	Knipovich JC094-S0071_CT	5.60	−26.97	1,990	0.086	1	0.003	Ng et al. (2020)	
61	Knipovich JC094-S0080_CT	5.59	−26.99	2,820	0.073	1	0.002	Ng et al. (2020)	
62	EW9209 3JPC	5.31	−44.26	3,300	0.049	1	0.001	Ng et al. (2018)	3
63	38GGC	4.90	−20.50	2,937	0.053	2	0.001	Lippold, Luo, et al. (2012)	
64	55GGC	4.90	−42.90	4,556	0.045	2	0.002	Lippold, Luo, et al. (2012)	3
65	58GGC	4.80	−43.00	4,341	0.045	3	0.009	Lippold, Luo, et al. (2012)	3
66	71GGC	4.40	−43.70	3,164	0.059	2	0.001	Lippold, Luo, et al. (2012)	3
67	82GGC	4.30	−43.50	2,816	0.049	3	0.004	Lippold, Luo, et al. (2012)	3
68	GeoB1515	4.24	−43.67	3,129	0.051	2	0.008	Süfke et al. (2019)	3
69	GeoB1523	3.83	−41.62	3,292	0.056	3	0.009	Süfke et al. (2019)	3
70	29GGC	2.50	−19.80	5,105	0.043	3	0.003	Lippold, Luo, et al. (2012)	
71	RC13-189	1.86	−30.00	3,233	0.054	3	0.003	Bradtmiller et al. (2007)	
72	RC16-66	−0.76	−36.62	4,424	0.043	3	0.002	Bradtmiller et al. (2007)	3
73	RC24-01	0.56	−13.65	3,837	0.042	2	0.001	Bradtmiller et al. (2007)	
74	V30-40	−0.20	−23.15	3,706	0.044	3	0.001	Bradtmiller et al. (2007)	
75	V22-182	−0.53	−17.27	3,614	0.034	3	0.010	Bradtmiller et al. (2007)	
76	RC24-07	−1.34	−11.92	3,899	0.044	3	0.001	Bradtmiller et al. (2007)	
77	RC24-12	−3.01	−11.42	3,486	0.045	3	0.002	Bradtmiller et al. (2007)	
78	GeoB16202-2	−1.91	−41.59	2,248	0.053	2	0.003	Mulitza et al. (2017)	3

Table 2
Continued

Index number	Core	Lat	Lon	Depth	Holocene (0–8 ka) Pa/Th	*n*	SE	Reference	Region
79	MD3253	−2.35	−35.45	3,867	0.042	1	0.002	Lippold et al. (2011)	3
80	MD3254	−2.80	−35.42	3,715	0.042	1	0.002	Lippold et al. (2011)	3
81	MD09-3256Q	−3.55	−35.38	3,537	0.047	1	0.002	Lippold et al. (2011)	3
82	MD3242	−4.22	−37.83	1,008	0.090	1	0.005	Lippold et al. (2011)	3
83	MD09-3257	−4.24	−36.35	2,344	0.067	3	0.006	Burckel et al. (2015)	3
84	GeoB3910	−4.25	−36.35	2,362	0.057	1	0.001	Waelbroeck et al. (2018)	3
85	GeoB1035-4	−21.60	5.03	4,450	0.031	1	0.001	Lippold, Luo, et al. (2012)	
86	GeoB1711-4	−23.34	12.38	1,967	0.123	3	0.006	Lippold, Luo, et al. (2012)	
87	GeoB3722-2	−25.25	12.02	3,506	0.065	3	0.001	Lippold, Luo, et al. (2012)	
88	C1 PC-ENG-111	−22.50	−40.10	621	0.097	1	0.003	Lippold, Luo, et al. (2012)	4
89	GeoB2117	−23.04	−36.65	4,045	0.049	1	0.001	Hickey (2010)	4
90	C2 PC-2121009	−24.30	−43.20	781	0.098	1	0.008	Lippold, Luo, et al. (2012)	4
91	GeoB 2107	−27.18	−46.45	1,048	0.076	6	0.006	Hickey (2010)	4
92	GeoB 2104	−27.29	−46.37	1,503	0.077	11	0.007	Hickey (2010)	4
93	KNR159-5 33GGC	−27.60	−46.20	2,082	0.074	6	0.007	This study	4
94	KNR159-5 17JPC	−27.70	−46.48	1,627	0.104	1	0.003	This study	4
95	GeoB2109	−27.91	−45.88	2,504	0.054	4	0.002	Hickey (2010)	4
96	KNR159-5 30GGC	−28.13	−46.07	2,500	0.066	5	0.003	This study	4
97	GeoB2112	−29.07	−43.22	4,010	0.051	4	0.001	Hickey (2010)	4
98	KNR159-5 22GGC	−29.47	−43.35	3,924	0.059	1	0.001	This study	4
99	AII107-09 117GGC	−30.84	−38.24	3,282	0.043	4	0.001	This study	4
100	MD02-2594	−34.28	17.33	2,440	0.067	11	0.005	Negre et al. (2010)	
101	ODP 1089	−40.94	9.89	4,621	0.049	12	0.004	Lippold et al. (2016)	
102	TN057-21	−41.10	7.80	4,981	0.050	2	0.002	Negre et al. (2010)	
103	MD02-2588	−41.20	25.50	2,907	0.050	2	0.002	Negre et al. (2010)	
104	PS2498-1	−44.15	−14.23	3,783	0.057	2	0.001	Anderson et al. (2014)	

Note. Index number refers to Figure 3a; region number refers to Figure 3b; ^{231}Pa/^{230}Th is the average of "*n*" samples in the time interval; SE is standard error. Individual samples are available at PANGAEA (Lippold et al., 2024).

2.5. Model Tuning of ^{231}Pa and ^{230}Th

We tuned the ^{231}Pa and ^{230}Th implementations to reflect modern seawater observations by varying the scavenging parameters. The realism of model simulations highly depends on these parameters: the 10 scavenging coefficients σ_i^j that determine adsorption, the 2 desorption constants k_{des}^j and the particle sinking speed w_s. Simulations with varying $\left(w_s, k_{des}^j, \sigma_i^j\right)$ were run for 5,000 years into steady state. The model-data agreement of each simulation was quantified by taking the weighted mean absolute error (MAE) for each of the four variables $^{231}Pa_d$, $^{230}Th_d$, $^{231}Pa_p$ and $^{230}Th_p$:

$$MAE\left(w_s, k_{des}^j, \sigma_i^j\right) = \frac{\sum_{l=1}^{N} a_l \cdot |sim_l - obs_l|}{\sum_{l=1}^{N} a_l}, \tag{11}$$

where $l = (\theta, \phi, z)$ is a grid cell where observations are present; with a weight $a_l = \frac{1}{e_l}$ with e_l the observational uncertainty; sim_l is the model simulation output and obs_l the measurement in grid cell l. Recall from Section 2.3 that multiple observations within one grid cell were averaged. We tuned ^{231}Pa and ^{230}Th by fixing the optimal

Table 3
Values of the Sinking Speed w_s, Desorption Constants k^j_{des}, and Scavenging Coefficients σ^j_i for: Three Parameter Sets Used for the Tuning of k^j_{des} (Figure S2 in Supporting Information S1); Minimum and Maximum σ^j_i of Observational Estimates (K^j_i From Chase et al. (2002), Geibert and Usbeck (2004), Hayes, Anderson, Fleisher, Vivancos, et al. (2015), S. Luo and Ku (2004a), and Zhang et al. (2021); Converted via Equation A9—See Tables S3 and S4 in Supporting Information S1); Values in Three Other Modeling Studies and in This Study

Parameter Unit	w_s m/yr	k^j_{des} /yr	σ^{Pa}_{POC} m^2/mol C	σ^{Pa}_{ca} m^2/mol C	σ^{Pa}_{op} m^2/mol Si	σ^{Pa}_{du} m^2/g dust	σ^{Pa}_{ne} m^2/g neph	σ^{Th}_{POC} m^2/mol C	σ^{Th}_{ca} m^2/mol C	σ^{Th}_{op} m^2/mol Si	σ^{Th}_{du} m^2/g dust	σ^{Th}_{ne} m^2/g neph
Tuning k^j_{des}: parameter set 1	1,000	*varies*	0.020	0.230	0.22	0.0044	0.028	0.084	3.97	0.110	0.0023	0.028
Tuning k^j_{des}: parameter set 2	1,400	*varies*	0.021	0.097	0.24	0.0028	0.026	0.210	1.73	0.029	0.0180	0.096
Tuning k^j_{des}: parameter set 3	1,600	*varies*	0.021	0.097	0.24	0.0028	0.026	0.210	1.73	0.029	0.0180	0.096
Min obs.	–	–	0.011	0.00007	0.00084	0.00001	0.00001	0.028	0.0023	0.0026	0.00009	0.00009
Max obs.	–	–	0.022	0.036	0.091	0.028	0.028	0.14	0.95	0.13	0.058	0.058
Marchal et al. (2000)	700	3.0	0.075	0.075	0.75	–	–	0.75	0.75	0.75	–	–
Rempfer et al. (2017)[a]	1,000	2.4	1	0.1	0.1	–	0.1	1	1	0.1	–	1
Missiaen, Bouttes, et al. (2020)[b]	1,000	2.4	1.55	0.22	3.17	–	–	5.47	9.21	1.57	–	–
This study (CTRL)	1,600	4.0	0.043	0.058	0.15	0.0031	0.029[c]	0.090	1.83	0.082	0.011	0.064

Note. Our σ^j_i tuning was performed from minimum obs. to twice maximum obs. [a]Values of σ^j_i are corrected for typos in their equations (see Appendix B). [b]Values of σ^j_i are converted to our units by multiplying with our M_i and dividing by the M_i in Missiaen, Bouttes, et al. (2020) (see caption of Table S4 in Supporting Information S1). [c]This parameter value is not well constrained by our tuning; the MAEs are not sensitive to it.

parameters in three steps: (a) w_s, (b) k^j_{des}, and (c) all σ^j_i. In the following we briefly describe the approach of these three steps (more information in Text S3 in Supporting Information S1), whereas the tuning results are discussed in Section 3.1.

First, we tuned the particle sinking speed w_s via an ensemble of 511 runs, in which all parameters $\left(w_s, k^j_{des}, \sigma^j_i\right)$ were varied. We only considered the MAEs of $^{231}Pa_p$ and $^{230}Th_p$ because they are directly related to w_s via the sinking term in Equation 6 (a change in w_s causes a change in A^j_p that subsequently affects A^j_d and this last step strongly depends on the σ^j_i values, which vary randomly in this ensemble, obscuring a clear comparison). We evaluate the performance of the w_s tuning ensemble by taking the normalized sum for each simulation:

$$MAE_{\mathrm{p},tot} = \frac{MAE_{\mathrm{Pap}}}{\overline{MAE_{\mathrm{Pap}}}} + \frac{MAE_{\mathrm{Thp}}}{\overline{MAE_{\mathrm{Thp}}}}, \tag{12}$$

where the bar indicates an average over all runs of this ensemble. Equation 12 was only used to determine w_s.

Subsequently, we established the best k^j_{des} (Figure S2 in Supporting Information S1). Instead of varying k^j_{des} in one ensemble, we varied it in three sub-ensembles with different fixed background parameter sets of w_s and σ^j_i (see Table 3) to explore how these affect the optimal k^j_{des}. For this tuning step we only evaluated MAE_{Pad} and MAE_{Thd}.

Finally, the σ^j_i were tuned in a 3,000-member ensemble with w_s and k^j_{des} fixed to the optimal values as determined in the previous tuning steps. This ensemble had more members, because in this step 10 parameters were tuned simultaneously. The limits of the parameter space of the partition coefficients K^j_i were derived from observational studies. These studies either performed laboratory experiments (Geibert & Usbeck, 2004; Zhang et al., 2021), used Atlantic seawater measurements from GEOTRACES (Hayes, Anderson, Fleisher, Vivancos, et al., 2015) or used sediment traps (Chase et al., 2002; S. Luo & Ku, 2004a). Their K^j_i estimates were converted to σ^j_i via Equation A9, and the minima and maxima are given in Table 3 (full compilation in Table S3 in Supporting Information S1). The lab measurements report lower K^j_i values than in situ measurements, with about an order of magnitude difference. The paper of Levier et al. (2022) was published after our tuning so is not included in this compilation. Their study estimates a value of K^{Pa}_{op} similar to Chase et al. (2002), thus not changing our results. The 3,000 runs were performed with all σ^j_i taken randomly from the range of minimum of observations to twice the maximum of observations using Latin hypercube sampling. We picked the σ^{Pa}_i values from the run that (a) is

Table 4
Main Model Runs in This Study

Runname	AMOC	Forcing[a]	Biological particles[b]	Description
CTRL	17.8 Sv	–	dyn.	Tuning result; CTRL = Pdyn_18Sv
Pdyn_14Sv	13.9 Sv	0.10	dyn.	Weaker AMOC (~14 Sv)
Pdyn_11Sv	11.2 Sv	0.15	dyn.	Weaker AMOC (~11 Sv)
Pdyn_9Sv	8.6 Sv	0.20	dyn.	Weaker AMOC (~9 Sv)
Px1_18Sv	17.8 Sv	–	fixed (×1)	CTRL with fixed particles
Px1_14Sv	13.9 Sv	0.10	fixed (×1)	~14 Sv AMOC with fixed particles
Px1_11Sv	11.2 Sv	0.15	fixed (×1)	~11 Sv AMOC with fixed particles
Px1_9Sv	8.6 Sv	0.20	fixed (×1)	~9 Sv AMOC with fixed particles
NO_NEPH	17.8 Sv	–	dyn.	No neph $\left(\sigma_{ne}^{j} = 0\right)$
NO_DUST	17.8 Sv	–	dyn.	No dust $\left(\sigma_{du}^{j} = 0\right)$

Note. Additional runs are given in Table C1. All simulations were run into steady state for 5,000 years. All runs have the same parameter settings, dust and nepheloid particles as CTRL, unless indicated otherwise. Biological particle fluxes consist of POC, $CaCO_3$ and opal. [a]Freshwater forcing [Sv] in the North Atlantic between 45° and 70°N. [b]Dynamically simulated (dyn.) or fixed to yearly avg. particles from CTRL (× a factor 1).

within the 10 runs giving the best MAE_{Pad} score, and (b) has the best MAE_{Pap} out of those 10 runs; analogously for ^{230}Th (Figure S3 in Supporting Information S1).

2.6. Model Simulations

Three types of runs were performed: runs for tuning (see Section 2.5), runs at pre-industrial (PI) steady state (e.g., CTRL; results in Section 3.1) and runs with variable AMOC and/or particle fluxes (results in Section 3.2). The most relevant model runs discussed in this study are listed in Table 4; additional experiments are in Table C1.

The default Bern3D spinup procedure is used to establish a steady state at pre-industrial conditions with $CO_2 = 278$ ppm and orbital conditions corresponding to 1765 CE, where the simulated ocean circulation is in equilibrium with the atmospheric energy-moisture balance module, and biogeochemical tracers (such as the nutrients needed for POC and opal) established their distribution throughout the ocean during 10,000 simulation years. The resulting AMOC maximum is 17.8 Sv and particle fluxes are simulated as shown in Figure 2. All simulations start from this steady state and run for 5,000 simulation years, except weak AMOC runs (see below).

The runs at pre-industrial steady state are: CTRL, NO_NEPH and NO_DUST. The control run (CTRL) contains the best-fit $\left(w_s, k_{des}^{j}, \sigma_i^{j}\right)$ result from the tuning. To examine the impact of our new model development, we perform two sensitivity runs: without nepheloid layers (NO_NEPH), and without dust (NO_DUST).

In model experiments called Pdyn_, Px_ and P/_, the AMOC and/or particle export fields are varied simultaneously. The AMOC is altered by applying a constant freshwater flux in the 45° to 70°N Atlantic.

In experiments with varying particles (Pdyn), changes in ocean circulation directly affect biological particle concentrations. This setup is used in the CTRL, Pdyn_14Sv, Pdyn_11Sv, and Pdyn_9Sv runs, whereas for runs with prefixes Px1_ and P/2_, Px2_ Px3_, and Px5_ (listed in Table C1) biological particle export fields are fixed to the yearly average of the particle flux fields obtained from the CTRL simulation (scaled by a factor). Although changes in the particle export pattern can change bottom $^{231}Pa_p/^{230}Th_p$ we choose to keep the pattern constant (only scaling the export) due to a lack of reliable reconstructions of past particle export.

To generate weakened AMOC states, we apply a continuous freshwater forcing to the North Atlantic (45°–70°N). The total freshwater amount is compensated for by a salt flux distributed over the rest of the surface ocean cells to avoid salt feedbacks elsewhere (Stocker et al., 2007). Freshwater forcings of 0.10, 0.15 and 0.20 Sv are applied, resulting in steady state AMOC strengths of 13.9, 11.2 and 8.6 Sv (78%, 63%, and 48% of the CTRL AMOC). Steady states with an AMOC weaker than 8.0 Sv are unfortunately not stable in the Bern3D model, as the addition of more freshwater causes a new steady state with a collapsed AMOC. The weakened AMOC state runs are run

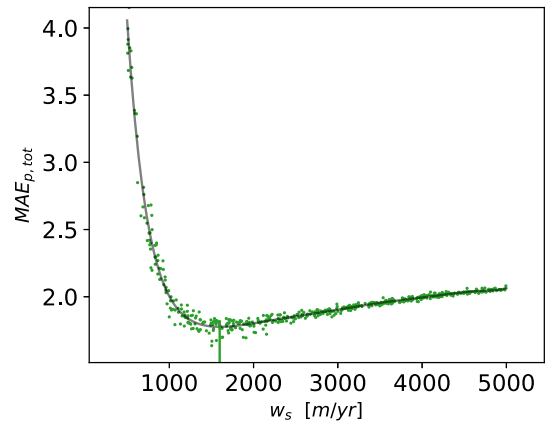

Figure 4. Particle-bound mean absolute error score function, as defined in Equation 12, as a function of sinking speed w_s. Every dot represents a model simulation of the 511-member ensemble that varies all parameters $\left(w_s, k^j_{des}, \sigma^j_i\right)$. A polynomial of degree 10 is fitted (solid line). The vertical line indicates its minimum, which yields the best value: w_s = 1,600 m/yr.

into equilibrium for 5,000 years and then used as starting points for the _14Sv, _11Sv, and _9Sv protactinium-thorium simulations (AMOC strengths are rounded in the suffixes), during which the freshwater forcings are still applied continuously.

3. Results and Discussion

3.1. Model Tuning and Comparison to Modern Data

Our multi-step tuning of simulated ^{231}Pa and ^{230}Th to modern seawater data provides important constraints. Figure 4 shows the result of the particle sinking velocity. A fitted polynomial was used to avoid dominance by outliers. Its minimum yields our tuning result for the sinking velocity: w_s = 1,600 m/yr. Larger w_s cause lower average $^{231}Pa_p$ and $^{230}Th_p$ because the particle-bound isotopes are removed more quickly by sinking particles. Hence, for large w_s, the MAE approaches an upper limit corresponding to the removal of virtually all $^{231}Pa_p$ and $^{230}Th_p$ ($sim_l = 0$ in Equation 11).

For the desorption constants, we only evaluate MAE_{Pad} and MAE_{Thd}, because MAE_{Pap} and MAE_{Thp} have very low sensitivity to k^j_{des} (not shown). The optimal k^j_{des} lie between 3.5 and 4.5/yr and depend on the parameter set (Figure S2 in Supporting Information S1). We conclude that k^{Pa}_{des} and k^{Th}_{des} are not significantly different and we take k^j_{des} = 4.0/yr as best value for both elements j. The last tuning step is described in Text S3 and Figure S3 in Supporting Information S1. The resulting tuned σ^j_i values are denoted in Table 3 as "This study (CTRL)." Our tuned results lie within the upper half of the observational range and often even above the observational maximum (recall that we sampled until twice the observational maximum). This supports the in situ measurements rather than the lab measurements, which reported lower values. Tuned σ^j_i values vary among studies and are compared between this study, Marchal et al. (2000), Rempfer et al. (2017), and Missiaen, Bouttes, et al. (2020) (Table 3). Generally, all studies suggest a stronger scavenging of ^{230}Th than of ^{231}Pa. The strongest ^{231}Pa scavenger is suggested to be opal in Marchal et al. (2000) and the present study, POC in Rempfer et al. (2017) and a combination in Missiaen, Bouttes, et al. (2020). The studies do not agree on the strongest ^{230}Th scavenger. Note that relative ratios were fixed in Rempfer et al. (2017) as only an overall factor was tuned. Missiaen, Bouttes, et al. (2020) report high values, because their tuning range started with high minimum values (see Text S3 in Supporting Information S1). Our study reports lower values than the other studies, probably because we added extra particles to the system (dust and nepheloid-layer particles).

Figure 5 shows the CTRL run output of annual average $^{231}Pa_d$, $^{230}Th_d$, $^{231}Pa_p$ and $^{230}Th_p$ together with seawater observations along two major Atlantic GEOTRACES transects, GA02 and GA03. Note that these transects were also part of the tuning data set. Figure C1 shows the same for more Atlantic transects (Deng et al., 2018, GA10, GIPY04 and GIPY05). Dissolved concentrations start out low in the northern North Atlantic along the GEOVIDE transect (Deng et al., 2018; Figure C1), both in the modeled CTRL and observations, as expected for newly

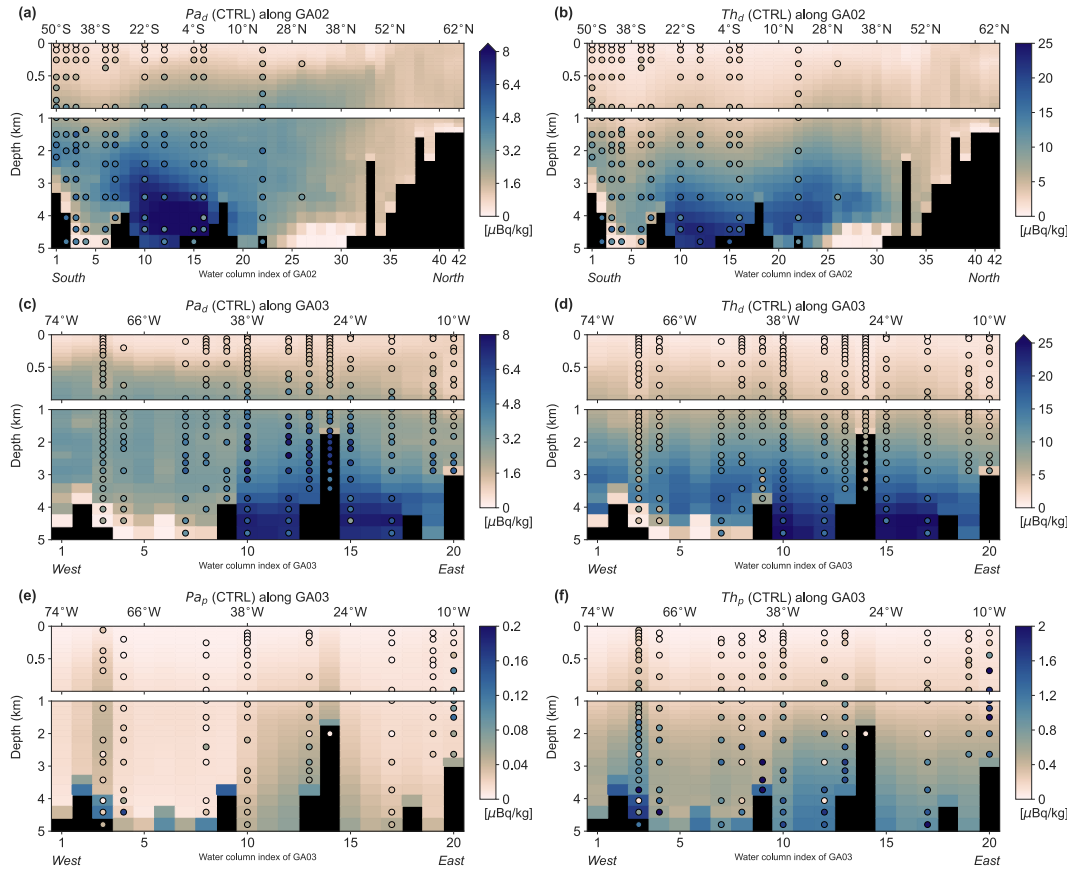

Figure 5. CTRL model output (background) with seawater observations (circles) along two large Atlantic transects: GA02 (a, b) and GA03 (c)-(f). Based on availability of measurements for $^{231}Pa_d$ (a, c), $^{230}Th_d$ (b, d), $^{231}Pa_p$ (e), and $^{230}Th_p$ (f). Data references in Section 2.3. See Figures 3c and 3d for trajectory maps of GA02 and GA03, which define the order of plotting and correspond to the water column indices on the *x*-axis. Seawater data circles are plotted centered in the nearest model grid cell box. If a grid cell contains multiple seawater observations, an uncertainty-weighted average is taken.

formed deep waters, because these waters were near the surface recently and therefore could only accumulate low concentrations. Along the meridional transect GA02 (Figures 5a and 5b), simulated and observed $^{231}Pa_d$ and $^{230}Th_d$ clearly show higher concentrations in the south, which originate from the accumulation of ^{231}Pa and (less so) ^{230}Th during transport by NADW advection. The effect of bottom scavenging is apparent in the low $^{231}Pa_d$ and $^{230}Th_d$ around the Bermuda Rise region and in the Argentine Basin, and is clearly too strong in the model compared to observations in the Argentine Basin. The CTRL, however, overestimates South Atlantic $^{231}Pa_d$ and $^{230}Th_d$ compared to GA02 measurements and possibly simulates their maximum concentrations not far south enough. The latter could be caused by a too strong modeled impact of nepheloid layers around the Argentine basin and Southern Ocean or by a too weak Antarctic bottom water circulation in the model compared to observations. Overall, modeled $^{231}Pa_d$ and $^{230}Th_d$ are too low in some regions and depth ranges of GA02 and too high in others. These model biases are better visible in Figures 6a and 6b—the scatter plot version of Figure 5. Here it becomes clear that modeled $^{231}Pa_d$ and $^{230}Th_d$ are too low compared to seawater observations almost everywhere along GA02, as most data points lie above the one-to-one line. This results in MAE values of 1.12 μBq kg^{-1} for $^{231}Pa_d$ and 2.77 μBq kg^{-1} for $^{230}Th_d$. In Figures 6a and 6b the largest bias to low values (ca. 7 data points in the upper lefts) comes from nepheloid layers in the Argentine Basin, whereas the largest bias to high values (12 and 2 data points in the lower rights) is located around 25°–0°S between 3 and 5 km. As visible in Figures 5a and 5b, this model-data discrepancy is strongest for $^{231}Pa_d$. Along GA02, measurements within one grid cell to the coastline (orange markers in the scatter plots) are not outliers. Least squares linear fits and their slopes (regression coefficients) are shown in each panel, but in many panels (especially for ^{231}Pa) outliers and the presence of both low and high biases make it impossible to find a satisfactory linear fit. Nevertheless, we provide the slopes here for

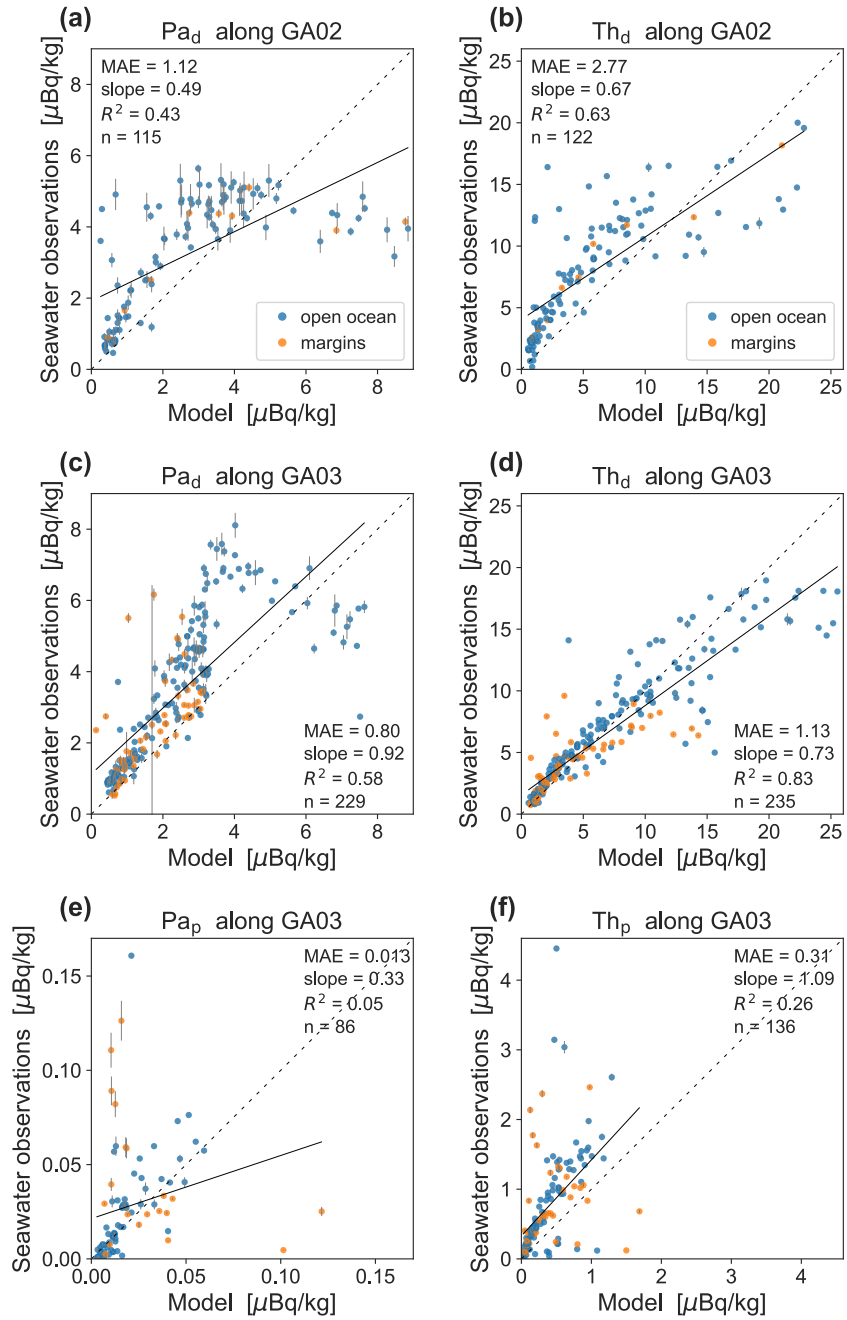

Figure 6. A scatter plot version of the model-data comparison in Figure 5; panels are in the same order. Orange markers indicate sites at the coastal margins (model grid cells adjacent to coast). The dashed line shows the one-to-one line of perfect correlation. The mean absolute error in μBq kg^{-1} is provided, weighted by observational uncertainties. The least squares linear fit is drawn (solid line), and its slope (regression coefficient), R^2 and number of data points are indicated. Seawater observations that lie deeper than the modeled ocean floor (as visible in Figure 5) are omitted. As in Figure 5, seawater data are averaged if a grid cell contains multiple seawater observations.

comparison to other studies (Dutay et al., 2009; Gu & Liu, 2017; Sasaki et al., 2022). For GA02, the model can only explain 43% of the observed variations in $^{231}Pa_d$ $(R^2 = 0.43)$ and 63% for $^{230}Th_d$.

The other major transect GA03, traversing the North Atlantic from west to east, shows a better fit with a gradient toward higher $^{231}Pa_d$ and $^{230}Th_d$ values in the east, both modeled and observed (Figures 5c and 5d). This concentration gradient between the deep western and eastern Atlantic is resolved in the Bern3D model simulations.

The R^2 and MAE values of the dissolved forms are better along GA03 (Figures 6c and 6d), with $R^2 = 0.58$ (MAE $= 0.80$ μBq kg^{-1}) for $^{231}Pa_d$ and $R^2 = 0.83$ (MAE $= 1.13$ μBq kg^{-1}) for $^{230}Th_d$. The case of $^{230}Th_d$ along GA03 has the best model-data agreement from all cases (panels) in Figure 6, with the one-to-one line almost going through the middle of the data cloud. Simulated $^{231}Pa_d$ and $^{230}Th_d$ are much lower than observed for a few grid cells (data points in upper left) in the deep Northwest Atlantic, which are located near the coastal margin or where strong nepheloid layers are present. The non-linearity of Figure 6c is caused by two strong model biases at 40°–20°W (east of the Mid Atlantic Ridge): modeled $^{231}Pa_d$ is too low there from ca. 1.5–3 km depth and too high from ca. 3.5–5 km depth (also visible in Figure 5c). The east-west gradient in protactinium and thorium concentrations along GA03 is also present in the particulate forms (Figures 5e and 5f). Bottom scavenging is visible again around the Bermuda Rise, with lowered dissolved concentrations and enhanced particulate concentrations near the ocean floor. The $^{231}Pa_p/^{230}Th_p$ ratio along GA03 (Figure C2) shows that this results in a modeled $^{231}Pa_p/^{230}Th_p$ increase in nepheloid layers. Overall, simulated $^{231}Pa_p/^{230}Th_p$ exhibits a vertical gradient with high values near the surface that decreases over depth. This expected behavior is not always present in the (scarce) seawater data available, resulting in a poor model-data fit in the surface ocean and a better fit at depth. Simulated $^{231}Pa_p$ and $^{230}Th_p$ clearly disagree with observations in about half of the measured water columns (Figures 5e and 5f). Both simulated particle-bound forms cannot reproduce the large variability in the observations between adjacent model water columns and depth layers. This results in broad scatter in the model-data comparison (Figures 6e and 6f) and a very poor R^2 of 0.05 (MAE $= 0.013$ μBq kg^{-1}) for $^{231}Pa_p$ and a poor R^2 of 0.26 (MAE $= 0.31$ μBq kg^{-1}) for $^{230}Th_p$. This is partially explained by strong mismatches of simulated with observational data at coastal margins (orange markers), where local conditions are not captured in the coarse resolution of the Bern3D model and the process of boundary scavenging, which is not implemented, may be relevant. Removing coastal data from the data set improves the performance to $R^2 = 0.39$ (MAE $= 0.009$ μBq kg^{-1}; $n = 66$) for $^{231}Pa_p$ and $R^2 = 0.44$ (MAE $= 0.28$ μBq kg^{-1}; $n = 100$) for $^{230}Th_p$. The other 4 data points with measured $^{230}Th_p$ higher than 2 μBq kg^{-1} are located around the Mid Atlantic Ridge and might be influenced by hydrothermal processes. In the Southern Ocean (GIPY04 and GIPY05 in Figure C1), modeled values are too low everywhere: on average 48% too low for $^{231}Pa_d$ and $^{230}Th_d$, 61% for $^{231}Pa_p$ and 72% for $^{230}Th_p$. The modeled $^{231}Pa_p/^{230}Th_p$ ratio along GIPY05 is generally too low compared to seawater observations, with large local variations (Figure C3) that may be caused by local variations in opal flux, which are hard to simulate and are a main control on Southern Ocean $^{231}Pa_p/^{230}Th_p$ (Gu & Liu, 2017). In a few water columns adjacent to the Antarctic coast, sea ice cover causes very low simulated $^{231}Pa_p/^{230}Th_p$ and unusual vertical gradients. For $^{230}Th_p$ we also recognize too little variation with depth in the Southern Ocean (Figure C1). This is probably caused by the simulated Southern Ocean opal belt being too narrow. A second cause is a too strong modeled impact of nepheloid layers (discussed below).

Next, we compare modeled $^{231}Pa_p/^{230}Th_p$ ratios to Holocene sediment $^{231}Pa/^{230}Th$ data, which were not used for the tuning. Simulated (ocean-floor) $^{231}Pa_p/^{230}Th_p$ generally reproduces the spatial pattern observed in sedimentary $^{231}Pa_p/^{230}Th_p$, except in regions with strong nepheloid layers (Figure 7a). Depths between model and sediment cores can differ because the model has the same water column depth within one grid cell, whereas sediment cores follow local bathymetry. This discrepancy explains the two outliers in the West Atlantic at 10° and 15°N, where the shallower sediment cores were located at a fracture zone and on a seamount (Ng et al. (2020): cores 48 and 49 (on top of each other in Figure 7a)) and core 38. The low values in Figure 7a illustrate that ^{231}Pa is exported out of the open Atlantic relative to ^{230}Th (blue; $^{231}Pa_p/^{230}Th_p$ below production ratio) toward the Southern Ocean (red; $^{231}Pa_p/^{230}Th_p$ above production ratio). The northern opal belt and the continental margins also experience an import of ^{231}Pa relative to ^{230}Th because of more abundant particles in this opal belt and in shallower regions, where less particles are remineralized. More quantitatively, Figure 7b shows considerable scatter in the model-data comparison of sedimentary $^{231}Pa/^{230}Th$ and an MAE of 0.023. The model explains only 35% of the variations in Holocene sediment cores. Nevertheless, there is no strong systematic bias with a slope close to 1. The sediment cores with $^{231}Pa/^{230}Th$ values higher than 0.15, which the model is not able to reproduce, are located in the upper 1.3 km at 0–20°N. Regionally, the model simulates too low $^{231}Pa_p/^{230}Th_p$ values compared to sedimentary reconstructions at 20°–40°N, and too high values in the equatorial Atlantic (10°S–10°N). The latter bias seems consistent with the too high $^{231}Pa_d$ (thus $^{231}Pa_p$) compared to seawater observations in the equatorial region of GA02.

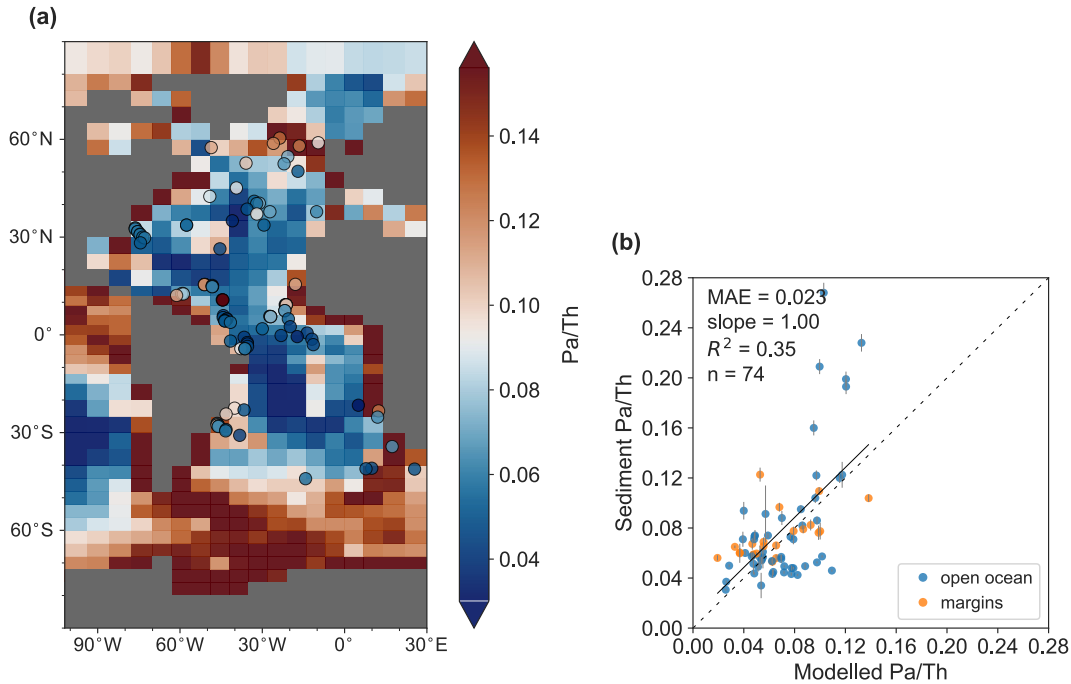

Figure 7. Model-data comparison of sedimentary $^{231}Pa/^{230}Th$. Model data are $^{231}Pa_p/^{230}Th_p$ ratios for the CTRL simulation. Sediment data are Holocene core-top $^{231}Pa_p/^{230}Th_p$ measurements from Figure 3a/Table 2. (a) Background colored squares: model data in the bottom ocean grid cells. Circles: sediment data. Values lower (higher) than the production ratio of 0.093 are blue (red) indicating ^{231}Pa export from (import to) that water column. If sediment cores are located close to each other, circles may fall behind other circles. (b) Sediment data compared to the closest model grid cell, which can lie in the model water column interior. Orange markers indicate sites at the coastal margins (model grid cells adjacent to coast). The dashed line shows the one-to-one line of perfect correlation. The mean absolute error (MAE; unitless) is provided, weighted by observational uncertainties. The least squares linear fit is drawn (solid line), and its slope (regression coefficient), R^2 and number of data points are indicated. Panel (a) uses all 104 cores, whereas panel (b) uses the subset where the model has values (i.e., sediment cores that lie deeper than the modeled ocean floor are omitted).

Now we examine the impact of our new model development concerning nepheloid layers and dust particles. The addition of benthic nepheloid layers largely improved $^{231}Pa_d$ and $^{231}Pa_p/^{230}Th_p$ in the Atlantic (Figure S5 in Supporting Information S1): the MAE metric compared to modern seawater data improved from 1.5 in NO_NEPH to 1.1 μBq kg^{-1} in CTRL for $^{231}Pa_d$ and from 0.044 to 0.031 μBq kg^{-1} for $^{231}Pa_p/^{230}Th_p$. However, for Atlantic $^{230}Th_d$ MAEs slightly increased from 2.0 to 2.2 μBq kg^{-1}, indicating a marginally worse fit. Since the tuning was performed over all ocean basins, regional differences exist, such that the CTRL results are not always better than NO_NEPH and NO_DUST in all basins and for all A_i^j simultaneously. The improvement of adding nepheloid layers in the Atlantic and Pacific comes at the cost of too low $^{231}Pa_d$ and $^{230}Th_d$ in the Southern Ocean, where NO_NEPH performs better than CTRL. This indicates a too strong impact of nepheloid layers in the Southern Ocean. In this region we filled nepheloid-layer data gaps with high values for nepheloid-layer thickness, which is confirmed by a recent study of eddy kinetic energy (Ni et al., 2023) implying strong nepheloid layers in the Southern Ocean (Gardner, Richardson, & Mishonov, 2018). Even though our nepheloid-layer maps (Figures 2e and 2f) seem plausible, it is possible that the modeled impact of nepheloid layers is still too strong via too thick nepheloid layers and/or too high values of σ_{ne}^{j} (recall that the tuning was not sensitive to σ_{ne}^{Pa}). In contrast, dust played a smaller role than nepheloid layers. Adding dust improved the match with seawater data in the regions of the Saharan and South American dust plumes (Figure 2d), leading to a small change in overall Atlantic MAEs (Figure S6 in Supporting Information S1). To conclude, these sensitivity tests emphasize that the potential impact of simulated nepheloid layers on deep ocean $^{231}Pa_p/^{230}Th_p$, $^{231}Pa_d$ and $^{230}Th_d$ can be large, even outside areas with strong nepheloid-layer presence, as was also found in Sasaki et al. (2022). In addition, adding dust particles improves the simulation in regions where dust plumes are prevalent.

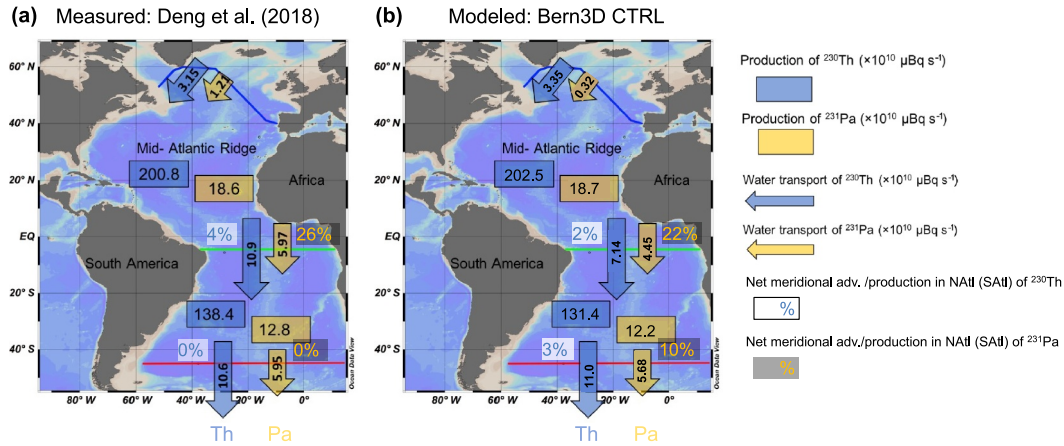

Figure 8. Budget of Atlantic ^{231}Pa (yellow) and ^{230}Th (blue) in μBq s^{-1} as computed (a) from observational estimates by Deng et al. (2018) and (b) from the Bern3D model CTRL run. Boundaries of the North and South Atlantic follow the transects GEOVIDE, WOCE A07 (4.5°S), and WOCE A11 (simplified version shown) (Deng et al. (2014); see Figure C4 for the transects on the Bern3D grid). Percentages express how much of the produced ^{231}Pa and ^{230}Th is exported out of the North or South Atlantic sub-basin by advection. The rest either sinks to the sediment within the sub-basin or is transported out of it by horizontal diffusion of ^{231}Pa and ^{230}Th. Adapted from Deng et al. (2018).

3.2. Detectability of the AMOC Signal in Sedimentary ^{231}Pa/^{230}Th

In this section, we first assess the budget of ^{231}Pa and ^{230}Th in the North and South Atlantic and compute their transport out of these sub-basins in the CTRL run. Then we test the detectability of AMOC changes in sedimentary $^{231}Pa_p/^{230}Th_p$ via model runs with varying AMOC states and/or particle export strengths.

First, we assess the budget of protactinium and thorium in the North and South Atlantic. We follow the approach of Deng et al. (2018), who computed meridional import and export fluxes of ^{231}Pa and ^{230}Th of the North and South Atlantic basins based on modern observations (Figure 8a). Deng et al. (2018) estimated that today 26% of the ^{231}Pa produced in the North Atlantic is exported out of it but only 4% of ^{230}Th, as can be seen from Figure 8a: $(5.97 - 1.21)/18.6 = 0.26$ and $(10.9 - 3.15)/200.8 = 0.04$. The authors interpreted the ca. 22% points difference between net North Atlantic ^{231}Pa and ^{230}Th export to be caused by the meridional transport of ^{231}Pa along NADW. For the South Atlantic the authors found no net import or export for both isotopes. After entering the Southern Ocean, most of ^{231}Pa finds its final sink in the Southern Ocean opal belt.

We perform the same budget analysis as Deng et al. (2018), now based on variables diagnosed from the Bern3D CTRL run (Figure 8b). The three transects were converted to the Bern3D grid (Figure C4) and their throughflow were computed similarly by diagnosing the horizontal velocities flowing through the section by using the adjacent $^{231}Pa_d$, $^{230}Th_d$ concentrations from the CTRL run (see Text S4 in Supporting Information S1 and results in Tables S1 and S2 in Supporting Information S1). Fluxes into the Mediterranean Sea were also computed but are negligible $\left(<0.01 \times 10^{10} \mu Bq/s\right)$. Overall, net results in the North Atlantic are similar between the Bern3D model and Deng et al. (2018): we find that 22% of ^{231}Pa produced in the North Atlantic is exported southward but only 2% of ^{230}Th. This consistency builds trust in the Bern3D model's large-scale circulation and implementation of protactinium-thorium. In the South Atlantic however, we find that 10% of ^{231}Pa is advected further southward, whereas Deng et al. (2018) estimated a net 0%. This net transport out of the South Atlantic results from a combination of southward transport in the west and northward transport in the east, where the latter is impacted by too low Southern Ocean $^{231}Pa_d$ and $^{230}Th_d$ concentrations in the Bern3D model compared to seawater observations (see Figure C1, top row) thereby impacting the net result.

While we draw no conclusions about the South Atlantic because of the model-observations discrepancy there, our findings confirm that present-day deep ocean circulation significantly fractionates ^{231}Pa and ^{230}Th in the North Atlantic. This clear difference between ^{231}Pa and ^{230}Th export out of the North Atlantic makes the present-day AMOC detectable at a sub-basin scale by averaging North Atlantic sediment measurements of Holocene $^{231}Pa_p/^{230}Th_p$ (see below). But are other AMOC states detectable as well?

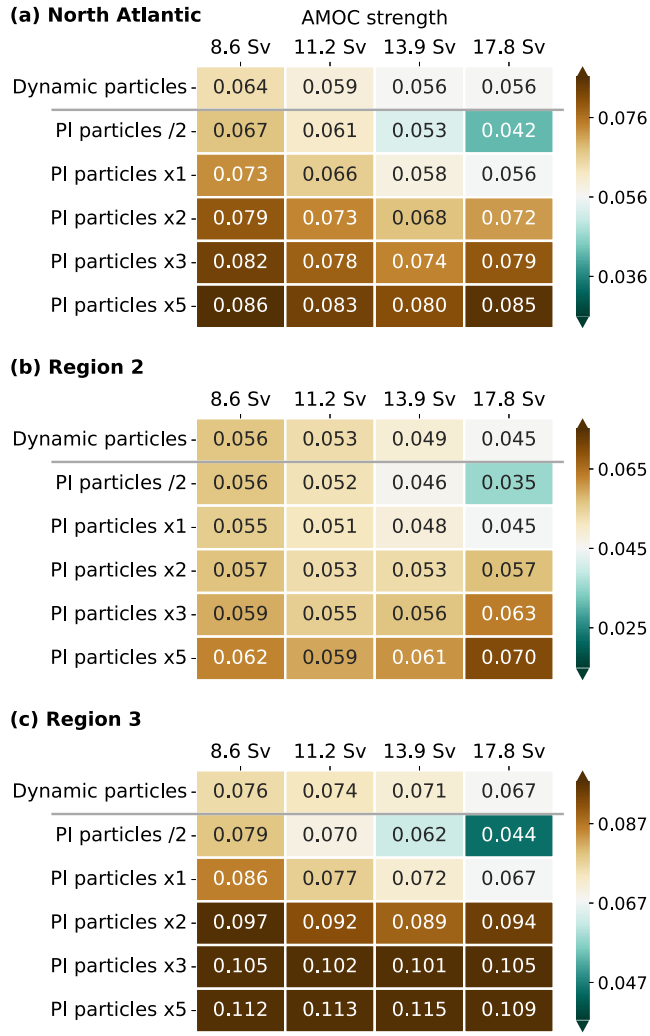

Figure 9. Heat maps of bottom $^{231}Pa_p/^{230}Th_p$ averaged over (a) the North Atlantic, (b) region 2 (the Bermuda Rise) and (c) region 3 (the equatorial West Atlantic). The average bottom $^{231}Pa_p/^{230}Th_p$ is used as a measure of Atlantic Meridional Overturning Circulation (AMOC) detectability in sediment. Simulations with varying AMOC (*x*-axes) and varying particle exports (*y*-axes) were used (Tables 4 and C1). Color bars are centered around the value of the CTRL run (light gray) in each panel. Changes between AMOC/particle export states that differ by at least 0.004 (a typical measurement uncertainty) are detectable in the respective region. The first row indicates runs where biogenic particles adjust dynamically to ocean circulation, whereas next rows keep particle export patterns fixed to the pre-industrial (PI) CTRL and scale the amount. Region boundaries are defined in Figures 3b and C4. Detectability heat maps for the other regions are given in Figure S8 in Supporting Information S1.

We further investigate the detectability under varying conditions using idealized model experiments with weakened AMOC and/or strengthened particle productivity. These experiments are sensitivity tests to understand the proxy's response to (extremely) different conditions. For instance last glacial maximum conditions are expected to lie within these ranges of AMOC strength and particle productivity (Abrantes, 2000; Lynch-Stieglitz et al., 2007; Mahowald et al., 2006; Schmiedl & Mackensen, 1997; Wollenburg et al., 2004). We choose the $^{231}Pa_p/^{230}Th_p$ ratio in bottom model grid cells averaged over a certain domain as a measure for the detectability of AMOC changes in sediment. Since Yu et al. (1996), this approach is often used by averaging over the entire Atlantic basin or the North Atlantic sub-basin. We average over the North Atlantic sub-basin (Figure 9a), because of the better model-data agreement in the budget assessment there compared to the South Atlantic. Recall that sub-basin boundaries are defined in Figure C4. As a threshold for significance we use the standard error of basin-mean sediment $^{231}Pa_p/^{230}Th_p$: 0.004, which is computed as the standard deviation of the 104 Holocene $^{231}Pa_p/^{230}Th_p$ values in Table 2 divided by $\sqrt{104}$.

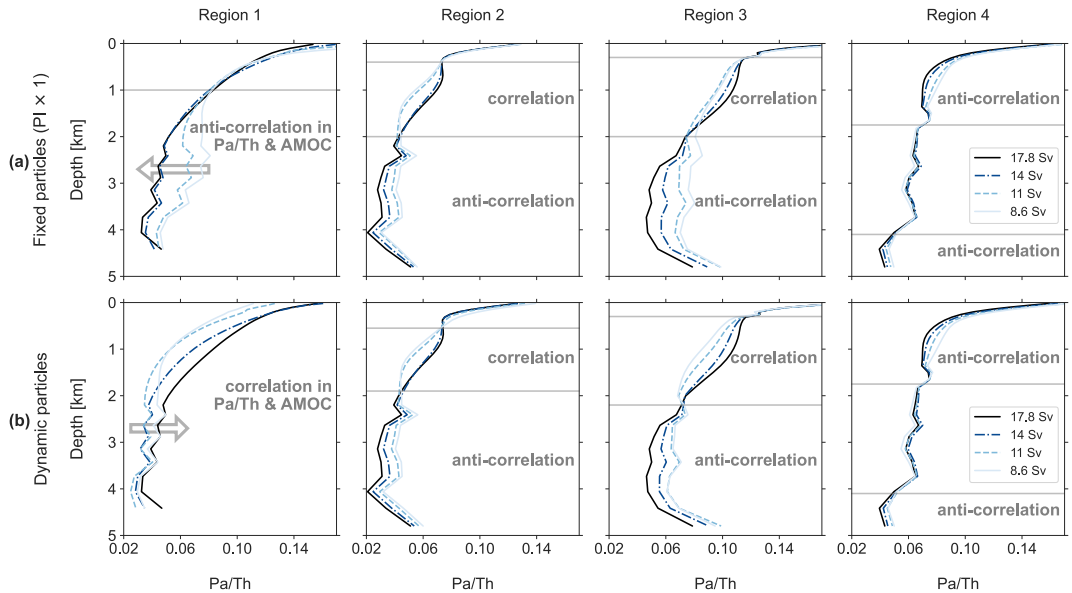

Figure 10. Modeled depth profiles of $^{231}Pa_p/^{230}Th_p$ in four regions of the West Atlantic, from north (region 1) to south (region 4; Figure 3b). (a) Runs Px1_18Sv, Px1_14Sv, Px1_11Sv, and Px1_9Sv with varying Atlantic Meridional Overturning Circulation (AMOC) and with biogenic particle fluxes fixed at the pre-industrial (PI) control. (b) Runs CTRL, Pdyn_14Sv, Pdyn_11Sv, and Pdyn_9Sv with varying AMOC and dynamically simulated biogenic particle fluxes, yielding more realistic simulation results. Arrows point in the direction of increasing modeled AMOC strength. Annotated text and gray lines demarcate domains with a recognizable anti-correlation between $^{231}Pa_p/^{230}Th_p$ and AMOC strength (arrow to left; black line left of blue lines) or a recognizable correlation (arrow to right; black line right of blue lines).

The resulting average $^{231}Pa_p/^{230}Th_p$ ratios are shown in the first row of Figure 9a for runs with varying AMOC and dynamically simulated particles (runs Pdyn_9Sv, Pdyn_11Sv, Pdyn_14Sv, and CTRL). The following rows (row 2–6) contain results from runs with varying AMOC and fixed biological particles. Depending on the row, particle exports are fixed to their CTRL state scaled by a factor of 0.5, 1, 2, 3 or 5 (runs are listed in Table C1). This way we vary AMOC (columns) and particle fluxes (rows) independently. We conclude that for each combination of AMOC state and particle export scaling a non-zero AMOC strength is detectable in North Atlantic bottom $^{231}Pa_p/^{230}Th_p$ (Figure 9a), since all values are lower than the production ratio 0.093 by at least 0.004. This implies that an 8.6 Sv AMOC state still imprints an AMOC signal on the North Atlantic $^{231}Pa_p/^{230}Th_p$ average, even if particle export is increased by as much as a factor of 5.

For the integrated North Atlantic region (Figure 9a) most changes between AMOC states are detectable (i.e., differ by at least 0.004) for biological particles scaled by /2, ×2, ×3 and ×5. However, for the relevant cases of dynamically simulated biological particles and for particles fixed to their pre-industrial distributions (PI particles ×1), AMOC strengths of 18 and 14 Sv (and 11 Sv) cannot be distinguished. Therefore, taking a simple (area-weighted) average over the North Atlantic seems not suitable to detect "non-extreme" changes between the present-day AMOC and AMOC strengths of at least ~12 Sv, but it seems suitable for extreme changes such as suggested during Heinrich Stadials. We will revisit this detectability measure with a more regional domain (Figures 9b and 9c) later in Section 3.3.

3.3. Causes for Correlation and Anti-Correlation Between $^{231}Pa/^{230}Th$ and AMOC

In the following, we classify which regions and depth ranges are believed to exhibit a positive correlation between $^{231}Pa_p/^{230}Th_p$ and AMOC strength (called correlation here) or a negative correlation (anti-correlation; as postulated for the Bermuda Rise; e.g., McManus et al. (2004)), and we attempt to understand the causes for this behavior with our model experiments. Figure 10 shows modeled depth profiles of $^{231}Pa_p/^{230}Th_p$ in four regions of interest in the West Atlantic, where sufficient sedimentary $^{231}Pa/^{230}Th$ observations are available (Figure 3b). These regions lie in the northern North Atlantic and at different latitudes of the West Atlantic. We focus on the West Atlantic in regions 2–4, since the strong and deep western boundary currents are expected to result in the clearest connection between sedimentary $^{231}Pa/^{230}Th$ and AMOC, in contrast to the Eastern Atlantic with its more

complex recirculation patterns and more water masses involved. We first consider region 1, a wider region in the northern North Atlantic, which covers the southern edge of the region where NADW formation takes place in the model, but also contains parts where NADW already undergoes horizontal advection. For fixed particle fields (panel a), weaker AMOC runs show higher $^{231}Pa_p/^{230}Th_p$ at depth, resulting in an anti-correlation between $^{231}Pa_p/^{230}Th_p$ and AMOC in region 1 (the northern North Atlantic). In contrast, the more realistic runs with dynamically simulated biological particles (panel b) result in a correlation instead, which is consistent with the positive correlation assumed in the interpretation of available sediment measurements (Gherardi et al., 2009; Süfke et al., 2020). Under AMOC weakening, less particles are present in region 1 (the northern North Atlantic), leading to lower surface $^{231}Pa_p/^{230}Th_p$ in Figure 10b compared to Figure 10a. These changes at the surface result in a shift of the weaker-AMOC profiles toward the left of the CTRL.

The reason for less particles in region 1 under AMOC weakening is that a weaker AMOC also reduces the transport of nutrients back to the 40°–60°N surface ocean, both via lessened lateral transport and via increased stratification, which reduces the mixing of surface waters with nutrient-rich deep waters (Schmittner, 2005). Therefore, this region becomes more limited by phosphate availability and export productivity decreases for POC, $CaCO_3$ and opal (Figures C5 and C6) (Nielsen et al., 2019). These lower particle fluxes cause a lower $^{230}Th_p$ and especially a lower $^{231}Pa_p$, resulting in a lower $^{231}Pa_p/^{230}Th_p$ in region 1 (the northern North Atlantic) in runs Pdyn_9Sv, Pdyn_11Sv, and Pdyn_14Sv compared to CTRL.

The particle response simulated in the Bern3D model takes nutrient transport and nutrient limitations by phosphate, silicate and iron into account, although the iron source (dust) is kept constant. Particle export could also be influenced by changes in remineralization rate and aggregation rates, which are not captured by the model. We compare the particle response in the Bern3D model with that in the CESM model (Gu & Liu, 2017). The results are only partially comparable, since Gu and Liu (2017) simulated a collapsed 1 Sv AMOC instead of our weakened 9 Sv AMOC. Particle export patterns in their AMOC-on state are similar to the Bern3D CTRL patterns for opal (with similar absolute values) and POC (with higher values in the Bern3D) but rather different for $CaCO_3$. Under AMOC weakening, both models simulate an overall particle flux decline in the northern North Atlantic, but the higher resolution CESM model shows a more detailed structure with the strongest opal and POC flux decrease in two subregions and an opal flux increase along the Greenland coast. Except for this feature, the patterns of particle response are roughly comparable between the models with a stronger absolute response in the Bern3D model.

Thus, in region 1, the effects associated with dynamical changes in biogenic particle flux enhance the signal from NADW advection in sediment $^{231}Pa_p/^{230}Th_p$—two processes that are generally assumed to partly cancel each other. At the low- to mid-latitude regions 2–4, modeled $^{231}Pa_p/^{230}Th_p$ depth profiles are strongly influenced by advection (Figure 10). Horizontal advection by NADW decreases $^{231}Pa_p/^{230}Th_p$ here, because NADW transports $^{231}Pa_d$ away (Burckel et al., 2016). The response of biological particles to AMOC change is small in regions 2–4 compared to region 1 (Figures C5 and C6) such that their depth profiles in Figure 10a resemble Figure 10b. When moving southward from region 2 to region 4, the $^{231}Pa_p/^{230}Th_p$ values in the CTRL run steadily increase at 2–4 km water depths, because we travel meridionally along with NADW advection, with $^{231}Pa_d$ thus $^{231}Pa_p$ continuously accumulating. $^{231}Pa_p/^{230}Th_p$ is especially low in region 2 (the Bermuda Rise region) because of too high simulated $CaCO_3$ fluxes inside the subtropical gyre and/or too strong nepheloid layers here. Even though modeled $^{231}Pa_p/^{230}Th_p$ is too low in region 2 compared to Holocene sediments, the relative changes between model runs in for example, Figure 10 are still meaningful, since nepheloid layers are temporally constant in the model. In the upper 2 km of the water column, we find a correlation in regions 2–3 (ignoring the surface layer) and an anti-correlation in region 4. Namely, in regions 2 and 3, the upper 2 km of the water column behaves opposite to the deeper ocean in its $^{231}Pa_p/^{230}Th_p$ response to AMOC strength. This is because the upper 2 km in the model are still governed by the upper limb of the AMOC, which transports water northwards and brings extra $^{231}Pa_d$ to the North Atlantic when the AMOC is strong (Gu & Liu, 2017).

Below 2 km, regions 2 (the Bermuda Rise region) and 3 (the equatorial West Atlantic) exhibit an anti-correlation, as expected, whereas region 4 (the Southwest Atlantic) has no detectable AMOC signal at these water depths, presumably due to the canceling effects of changes in dissolved ^{231}Pa import and ^{231}Pa export here. In the deepest kilometer, an increase in $^{231}Pa_p/^{230}Th_p$ can be interpreted either as Antarctic bottom water and/or as bottom scavenging. Antarctic bottom water brings in water with a higher $^{231}Pa_p/^{230}Th_p$ coming from the south below ca. 4 km depth. Bottom scavenging increases $^{231}Pa_p$ and $^{230}Th_p$ concentrations in the nepheloid layer. Since the

fractionation between ^{231}Pa and ^{230}Th is small in nepheloid layers (fractionation factor 2 in our tuning; Table 3) compared to a typical mix of particle types (including $CaCO_3$ with fractionation factor 30), $^{231}Pa_p/^{230}Th_p$ values increase in nepheloid layers (Hayes, Anderson, Fleisher, Huang, et al., 2015). Note from Figures 2e and 2f that nepheloid-layer height and intensity are particularly large in region 2 (Bermuda Rise), explaining the clear $^{231}Pa_p/^{230}Th_p$ increase at 4–5 km there. Region 3 (the equatorial West Atlantic) is somewhat more sensitive to AMOC changes at depth than region 2 (the Bermuda Rise), especially to an AMOC decrease from 18 to 14 Sv. Therefore, we propose that sediment ^{231}Pa/^{230}Th records from the equatorial West Atlantic deserve as much attention as those from the Bermuda Rise, with the advantage of a smaller contribution from bottom scavenging.

We assess the detectability in the promising regions 2 and 3, where bottom $^{231}Pa_p/^{230}Th_p$ is spatially averaged over those regions (Figures 9b and 9c). Region 3 (the equatorial West Atlantic) can detect the difference between 14 and 18 Sv AMOC states (i.e., they differ by at least 0.004), which is not the case in the North Atlantic average at present-day levels of particle export (Figure 9a). This AMOC difference is also detectable in Region 2 (the Bermuda Rise) for dynamic particles but not for particles fixed to their pre-industrial distributions (PI particles $\times$1). The $^{231}Pa_p/^{230}Th_p$ ratios in region 2 (the Bermuda Rise) are too low compared to sediment observations, because of too strong simulated nepheloid layers and/or $CaCO_3$ export there (Section 3.1), such that only the relative changes of Figure 9b are useful when comparing to sedimentary reconstructions. Model-data agreement is substantially better in region 3 (the equatorial West Atlantic) such that present-day absolute values in Figure 9c are more reliable. For PI particles $\times$1 and PI particles /2, region 3 performs best in detecting AMOC changes, with easily detectable steps in bottom $^{231}Pa_p/^{230}Th_p$ of 0.005 and more, but for dynamic particles (most realistic) the detectability in regions 2 and 3 is similar. In all regions (Figures 9a–9c), particles $\times$2, $\times$3 and $\times$5 scenarios show a local minimum in bottom $^{231}Pa_p/^{230}Th_p$ at 11 or 14 Sv due to an interaction between AMOC strength and particle effects. Variations in bottom $^{231}Pa_p/^{230}Th_p$ are hard to attribute in these cases such that AMOC changes between 11 and 18 Sv at a doubling of particle export are not detectable. To summarize, we conclude that at present-day levels of particle export the AMOC is better detectable in $^{231}Pa_p/^{230}Th_p$ averaged over region 2 or 3 than in an entire North Atlantic average. Detectability heat maps for the other regions are provided in Figure S8 in Supporting Information S1. Region 4 is not suitable; region 1 can potentially be used in the future but further sediment cores and modeling studies are needed to assess the Bern3D $^{231}Pa_p/^{230}Th_p$ depth profiles there.

The response of $^{231}Pa_p/^{230}Th_p$ to a reduced AMOC is summarized in Figure 11 along the Atlantic GEOTRACES transects GA02 and GA03. In red (blue) regions, the 9 Sv run has higher (lower) $^{231}Pa_p/^{230}Th_p$ than the 18 Sv run, corresponding to a negative (positive) correlation between $^{231}Pa_p/^{230}Th_p$ and AMOC. Local strong bottom scavenging causes high values in a few bottom water grid cells. The GA03 transect (Figures 11c and 11d) shows that east-west differences are minor, except close to the West African coast, where biogenic particle fluxes are high. As in Figure 10, the most striking impact of the particle response along GA02 (Figures 11a and 11b) is visible at 40°–60°N (region 1), which is the region with the strongest change in particle fluxes. The strong negative anomaly at 40°–55°N for dynamic particles (Figure 11b) is a result of the reduced export productivity there in Pdyn_9Sv: particle fluxes of POC, $CaCO_3$, and especially fluxes of biogenic opal are reduced (virtually no northern opal belt is present anymore). This causes a large change in $^{231}Pa_p/^{230}Th_p$ compared to CTRL at the northern opal belt location. The weak correlation (light blue) throughout the South Atlantic is caused by the South Atlantic being the constant destination of ^{231}Pa imported from the north. Namely, the CTRL AMOC state produces a small but discernible gradient in $^{231}Pa_p/^{230}Th_p$ from north to south in the deep ocean (in absence of local particle effects; see Figure 5). A weaker AMOC state advects less $^{231}Pa_d$ such that this gradient lessens. In other words, under AMOC weakening, more $^{231}Pa_d$ stays near the radioactive production site (increasing $^{231}Pa_p/^{230}Th_p$ in the North Atlantic hence an anti-correlation) and less additional $^{231}Pa_d$ arrives in the South Atlantic (decreasing $^{231}Pa_p/^{230}Th_p$, hence a correlation). The darkest colors in Figure 11b indicate the latitudes and depths most promising for using sediment ^{231}Pa/^{230}Th as an AMOC proxy—although east-west differences may still exist and the Bern3D model results are not reliable around coastal margins. This reveals that additional sediment cores between 40° and 60°N and 1–2 km depth could be very promising. The few existing downcore ^{231}Pa/^{230}Th records from this region often record large changes in opal between the Holocene and the last glacial maximum (Gherardi et al., 2009; Hall et al., 2006) such that they have not been used to infer AMOC signals until now. The way how POC, $CaCO_3$ and opal fluxes respond to a weaker AMOC enables us to reconstruct AMOC changes from sediment ^{231}Pa/^{230}Th in a different way in this region. However more

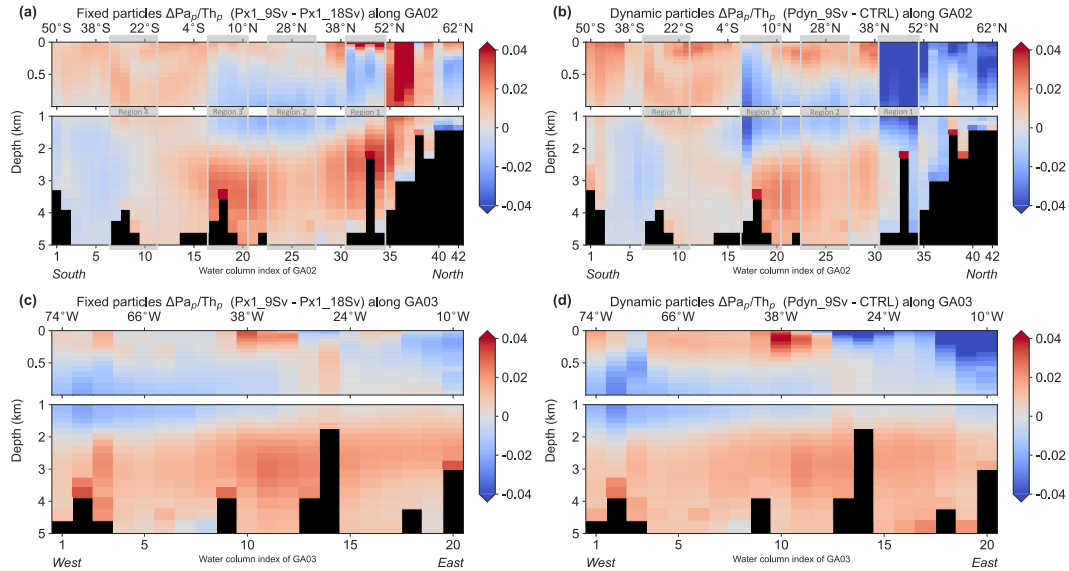

Figure 11. Response of modeled $^{231}Pa_p/^{230}Th_p$ to a ~50% Atlantic Meridional Overturning Circulation (AMOC) weakening along the two major Atlantic transects: GA02 in the upper panels (a), (b) and GA03 in the lower panels (c), (d). Red indicates increasing $^{231}Pa_p/^{230}Th_p$ when AMOC decreases, and blue indicates decreasing $^{231}Pa_p/^{230}Th_p$ when AMOC decreases. The result is shown for fixed particles (PI particles × 1) in the left panels (a), (c) by subtracting run's Px1_18Sv $^{231}Pa_p/^{230}Th_p$ from that in Px1_9Sv, and for dynamic particles in the right panels (b), (d), where CTRL = Pdyn_18Sv. See Figures 3c and 3d for trajectory maps of GA02 and GA03.

modeling studies investigating this effect would be beneficial in order to assess the reliability of the particle response in the Bern3D model.

Previous modeling studies also assessed the response of sedimentary $^{231}Pa/^{230}Th$ to variations in AMOC (Gu & Liu, 2017; Gu et al., 2020; Marchal et al., 2000; Missiaen, Bouttes, et al., 2020; Rempfer et al., 2017). These studies generally forced the simulated AMOC into its off-state, allowing only for a limited comparability to our 9 Sv AMOC circulation state. Nevertheless, they found similar results to the ones described here, exhibiting an anti-correlation in the deep Atlantic from about 30°S to 40°N and a positive correlation in parts of the deep 40°–80°N Atlantic. In the northern North Atlantic, the results by Missiaen, Bouttes, et al. (2020) resemble our simulated fixed-particles response, whereas previous results from the Bern3D model (Rempfer et al., 2017; Süfke et al., 2020) are similar to the dynamic-particles case. However, the findings by Gu and Liu (2017) are remarkably different from ours and show less difference between fixed-particles and dynamic-particles simulation results for North Atlantic bottom $^{231}Pa_p/^{230}Th_p$ compared to that difference in the Bern3D model. This is presumably because Gu and Liu (2017) consider an AMOC shutdown state, which results in a different circulation and a partially different particle response (see Section 3.2). Gu and Liu (2017) also investigated the time dependence of the sediment $^{231}Pa/^{230}Th$ response to a circulation change with accompanying dynamic changes in biogenic particle fluxes. They found that changes in biogenic particle fluxes affect $^{231}Pa_p/^{230}Th_p$ fastest, followed by the impact of AMOC change later in time. After equilibrium was established, the AMOC signal dominated over the particle signal in most regions, except at 40°N, 40°W, 4,375 m, where they found a slight positive correlation between AMOC strength and sediment $^{231}Pa/^{230}Th$ as a result of the particle response. This qualitatively agrees with our results, as we only analyzed equilibrium states and since their location of slight positive correlation lies close to where we find positive correlations in region 1 (northern North Atlantic; Figure 11b).

Based on our model experiments, it emerges that the relationship between AMOC strength and $^{231}Pa_p/^{230}Th_p$ is non-linear because AMOC changes are also directly linked to corresponding changes in particle concentrations also affecting $^{231}Pa_p/^{230}Th_p$. When the AMOC weakens, detecting the reduced NADW advection in sediment $^{231}Pa/^{230}Th$ records becomes challenging, although the induced particle response partly compensates for this and amplifies the effect of AMOC on sediment $^{231}Pa/^{230}Th$ in the northern North Atlantic. On the other hand, when the AMOC strengthens, the signal from NADW advection is large, but the particle response with

enhanced export production partly counteracts this and dampens the detectability. Those opposing effects of circulation changes and their induced particle response are also discussed in Missiaen, Menviel, et al. (2020) and Gu and Liu (2017).

4. Conclusions and Outlook

We improved the $^{231}Pa/^{230}Th$ module of the Bern3D model by adding dust and spatially varying nepheloid layers (bottom scavenging), and we extensively retuned the particle sinking speed w_s, the 2 desorption constants k^j_{des}, and 10 scavenging parameters σ^j_i. The resulting CTRL simulation was compared to present-day seawater observations and Holocene sediment core tops in the Atlantic. The MAE between simulated and sedimentary bottom $^{231}Pa/^{230}Th$ is 0.023. The CTRL simulation performs best in the open ocean, and less well in coastal margins and in regions with strong nepheloid layers (Southern Ocean sector; Bermuda Rise). Model experiments with different AMOC strengths and particle flux distributions demonstrate that a North Atlantic average of bottom $^{231}Pa/^{230}Th$ can always detect a non-zero NADW advection, but cannot distinguish between ∼12 and 18 Sv AMOC states. Extreme changes when the AMOC is reduced by at least 7 Sv are still detectable in the North Atlantic average. Averaging bottom $^{231}Pa/^{230}Th$ over the Bermuda Rise region or equatorial West Atlantic instead allows for distinguishing 11, 14 and 18 Sv AMOC states. We suggest that region 2 or 3 is used, depending on the time period of study and the available knowledge of past particle changes. For a factor 2 increase in particle export, the relationship between AMOC strength and bottom $^{231}Pa/^{230}Th$ becomes non-monotonic between 11 and 18 Sv in the Bern3D model, suggesting that AMOC changes are not detectable in $^{231}Pa/^{230}Th$ in that regime.

The response of particulate $^{231}Pa/^{230}Th$ to AMOC in different regions and depths of the Atlantic was explored in the model. The conclusions of this study only apply to sediment cores outside the coastal margins, where the Bern3D model does not simulate $^{231}Pa_p$ and $^{230}Th_p$ well (see Section 3.1). In the Bern3D model, AMOC strength is anti-correlated with $^{231}Pa/^{230}Th$ in the deep equatorial West Atlantic and Bermuda Rise. The Bermuda Rise sediment $^{231}Pa/^{230}Th$ records are commonly considered as reference indicators for past changes in AMOC, but both regions deserve attention, especially since the equatorial West Atlantic does not suffer from strong bottom scavenging and the resulting uncertainties in past bottom scavenging strength. In the South Atlantic, the modeled $^{231}Pa/^{230}Th$ seems to be insensitive to AMOC changes, which could be caused by model biases. Lastly, the northern North Atlantic (region 1) possesses a positive correlation between $^{231}Pa/^{230}Th$ and AMOC strength in the model. The reason for this positive correlation is a strong AMOC-induced particle response here—this is the only difference between the simulations in Figures 10a and 10b. A weaker AMOC transports less nutrients to the surface in region 1 (reduced lateral transport and reduced mixing with deep waters), which leads to fewer particles and lower bottom $^{231}Pa_p/^{230}Th_p$ in this region. Thus, changes in ocean circulation and changes in biogenic particle fluxes caused by those circulation changes produce opposite effects here on bottom $^{231}Pa_p/^{230}Th_p$. Cores in this region with high opal from the northern opal belt are actually promising for the reconstruction of AMOC variations when we embrace their positive correlation between $^{231}Pa/^{230}Th$ and AMOC in (part of) the 40°–60°N Atlantic.

Despite certain knowledge gaps, sediment $^{231}Pa/^{230}Th$ records present a high potential to reliably quantify past AMOC changes. To overcome these knowledge gaps, more modeling studies on the factors influencing the oceanic distributions of ^{231}Pa and ^{230}Th are needed, focused on the same goals as ours (see below). Further, additional sediment cores between 40° and 60°N and between water depths of 1 and 2 km in the Atlantic Ocean are desirable, especially close to locations of known positive correlation (such as cores 10, 11, and 13; Figure 3a). A reinterpretation of downcore records recovered from regions 1, 2, and 3 should be performed based on the new insights gained in this study and future modeling studies.

Possibilities for follow-up studies with the Bern3D model are: (a) find a better way to tune σ^j_{ne}, the coefficients of scavenging to nepheloid-layer particles (Table 3); (b) investigate a collapsed AMOC state, which exhibits a very different circulation; and (c) make particle sinking speed and remineralization more realistic. In the model version employed here, both sinking speeds and remineralization profiles are globally uniform. For remineralization, particle types have different remineralization profiles with different typical depth scales (Equations 2–4), but these are globally uniform instead of depending on local characteristics such as temperature and oxygen concentration. For particle sinking, a universal sinking speed w_s is assumed that only affects the geochemical tracers. Ideally, models would distinguish particle types of different sizes with different sinking speeds, depending on

typical particle size and density. This is for example, implemented in the NEMO model (van Hulten et al., 2018) but not yet in the Bern3D model. Since ^{230}Th has a higher affinity to smaller particles than ^{231}Pa has (Kretschmer et al., 2011), the current bulk sinking speed of w_s = 1,600 m/yr hampers a realistic process-based simulation of ^{231}Pa and ^{230}Th, limited by the simplified description of particle fluxes in the model. The realism of both sinking speeds and remineralization can be improved by coupling to the new particle flux model MSPACMAM (Dinauer et al., 2022). We note that changing sinking speeds requires a new tuning (or a simple rescaling) of the scavenging coefficients, since altered sinking speeds change the effective particle abundance, and sensitivity tests showed that simulated $^{231}Pa_p/^{230}Th_p$ is highly sensitive to the sinking speed (not shown).

Modeling studies use widely different scavenging parameters, either found by tuning or chosen from the wide range of observational literature (Table S3 in Supporting Information S1). It would be important to better constrain the ranges of scavenging parameters, which would also improve the comparability between studies. Here the absolute values are not of much importance, but the ratios between the parameters are. Computationally more expensive models could still perform many steady state tuning runs by using Anderson Acceleration (Khatiwala, 2023). An alternative to tuning is taking over the scavenging parameter set from another modeling study if this directly yields satisfactory protactinium-thorium results in the model at hand (not only for the $^{231}Pa_p/^{230}Th_p$ ratio but also for the separate dissolved and particulate phases). Scavenging coefficients and partition coefficients can be converted into each other as shown in Table S4 in Supporting Information S1.

More modeling studies of weakened AMOC states are also desirable to confirm the large potential we saw in the equatorial West Atlantic, and to assess the particle response to an AMOC weakening in the Bern3D model. If another model performs better in region 1 (i.e., if the modeled $^{231}Pa_p/^{230}Th_p$ depth profile fits well with Holocene sediment ^{231}Pa/^{230}Th data), then this model could be used to quantify how much AMOC decline a certain decrease in northern North Atlantic sediment ^{231}Pa/^{230}Th corresponds to. If the same model also reproduces Holocene sediment data in regions 2 and 3, like the Bern3D model, then the AMOC detectability could be quantified there as well.

In conclusion, we have presented a detailed modeling study, combined with new sediment ^{231}Pa/^{230}Th measurements, and provided a new regional-scale analysis of detectability of AMOC changes by this paleoceanographic tracer. Combining it with other tracers will further enhance its usefulness in reconstructing past ocean circulation changes and their regional signals.

Appendix A: The Diagnostic and Prognostic Approaches of Modeling ^{231}Pa and ^{230}Th

In this section, we clarify the two most common approaches of implementing ^{231}Pa and ^{230}Th in three-dimensional models with a dynamical description of ocean circulation, but their difference is rarely explained. We name these two approaches diagnostic and prognostic approach according to their treatment of particle scavenging in the governing equations (see below). Diagnostic refers to the approach of determining (diagnosing) dissolved and particulate tracer concentrations from a simulated total concentration.

The governing equations of the diagnostic approach are (e.g., Gu & Liu, 2017):

$$\frac{\partial A^j_{\text{total}}}{\partial t} = \text{Transport}\left(A^j_{\text{total}}\right) - \lambda^j A^j_{\text{total}} + \beta^j - w_s \frac{\partial A^j_p}{\partial z}, \tag{A1}$$

with

$$A^j_d = \frac{1}{1 + \frac{1}{\rho_{sw}}\left(K^j_{\text{POC}} C_{\text{POC}} + K^j_{\text{ca}} C_{\text{ca}} + K^j_{\text{op}} C_{\text{op}} + K^j_{\text{du}} C_{\text{du}}\right)} \cdot A^j_{\text{total}}, \tag{A2}$$

$$A^j_p = \left(1 - \frac{1}{1 + \frac{1}{\rho_{sw}}\left(K^j_{\text{POC}} C_{\text{POC}} + K^j_{\text{ca}} C_{\text{ca}} + K^j_{\text{op}} C_{\text{op}} + K^j_{\text{du}} C_{\text{du}}\right)}\right) \cdot A^j_{\text{total}}, \tag{A3}$$

whereas the prognostic approach is formulated as (e.g., Rempfer et al., 2017):

$$\frac{\partial A_d^j}{\partial t} = \text{Transport}\left(A_d^j\right) - \lambda^j A_d^j + k_{\text{des}}^j A_p^j - k_{\text{ads}}^j A_d^j + \beta^j, \tag{A4}$$

$$\frac{\partial A_p^j}{\partial t} = \text{Transport}\left(A_p^j\right) - \lambda^j A_p^j - k_{\text{des}}^j A_p^j + k_{\text{ads}}^j A_d^j - w_s \frac{\partial A_p^j}{\partial z}. \tag{A5}$$

It is evident that the prognostic approach is physically more realistic as it simulates the different processes individually. The advantage of the diagnostic approach on the other hand is that it is computationally lighter.

Variables and parameters are listed in Table 1 of the main text. The tracers are subject to oceanic transport (advection, convection and diffusion). Sources and sinks are radioactive decay, radioactive production, and scavenging by particles sinking with speed w_s. The approaches simulate reversible scavenging by sinking particles differently. The diagnostic approach uses particle mass concentrations C_i, seawater density ρ_{sw} and fixed partition coefficients, or distribution coefficients, $(K_d)_i^j = K_i^j$, which govern the ratio of particle-bound to dissolved concentration (Gu & Liu, 2017):

$$K_i^j = \frac{\rho_{sw}}{C_i} \frac{A_{p,i}^j}{A_d^j} \tag{A6}$$

$$i \in [POC, CaCO_3, opal, dust, neph]$$
$$j \in [^{231}\text{Pa}, ^{230}\text{Th}]$$

with $A_{p,i}^j$ the part of A_p^j that is bound to particle type i. Particle types i vary between studies, especially whether dust and nepheloid-layer particles are present. The prognostic approach instead simulates scavenging via adsorption and desorption coefficients:

$$k_{\text{ads}}^j(\theta, \phi, z) = \sum_i \sigma_i^j \cdot F_i(\theta, \phi, z), \tag{A7}$$

$$k_{\text{des}}^j = \text{constant}, \tag{A8}$$

$$i \in [POC, CaCO_3, opal, dust, neph]$$
$$j \in [^{231}\text{Pa}, ^{230}\text{Th}]$$

where σ_i^j are globally uniform scavenging coefficients expressing how strongly particle type i adsorbs tracer j, and where $F_i(\theta, \phi, z)$ is the settling flux of particle type i at grid cell (θ, ϕ, z). The scavenging parameters of the two approaches (partition coefficients K_i^j and scavenging coefficients σ_i^j) can be converted into one another via Missiaen, Bouttes, et al. (2020):

$$K_i^j = \frac{w_s \cdot \rho_{sw} \cdot \sigma_i^j}{M_i \cdot k_{des}^j}, \tag{A9}$$

where M_i is the molar conversion factor for particle type i. This relationship allows us to compare results between all studies. For this comparison (Table 3), we use the molar conversion factors assumed in the Bern3D model: $M_{POC} = M_{ca} = 12$ g/mol (simulated in mol C), $M_{op} = 28$ g/mol (simulated in mol Si) and $M_{du} = M_{ne} = 1$ (dust and nepheloid-layer particles are already simulated in g).

The diagnostic approach was introduced by Henderson et al. (1999) in the HAMOCC model and was used in the Bern3D model (Siddall et al., 2005), the NEMO model (Dutay et al., 2009; van Hulten et al., 2018), the CESM (Gu & Liu, 2017) and the COCO model (Sasaki et al., 2022). The prognostic approach was introduced by Marchal et al. (2000) and is applied in the Bern3D model (Rempfer et al., 2017), the POM (Princeton Ocean Model; Lerner et al. (2020)) and the iLOVECLIM model (Missiaen, Bouttes, et al., 2020). The approaches are not equivalent, and both have their advantages and disadvantages. The diagnostic approach has the advantage that (a) the

computational cost is reduced; and (b) the usage of K_i^j is analogous to common implementations of other paleoceanographic tracers such as neodymium (Arsouze et al., 2009; Gu et al., 2019; Rempfer et al., 2011) and beryllium (Heinze et al., 2006; Li et al., 2021). On the other hand, the prognostic approach allows for disequilibrium between adsorption and desorption. Although desorption-adsorption equilibrium already establishes on the order of several months (Bacon & Anderson, 1982), this can make a difference in regions where, for example, seasonal effects are important, for instance during deep water formation.

Appendix B: Corrections to Equation in Rempfer et al. (2017)

The tuning results from this study were compared to those from Rempfer et al. (2017) in Table 3 of the main text, where we corrected their results for typos in their equations, as explained here. Rempfer et al. (2017) define the fractionation factor as $f_i = f_i(Th/Pa) = K_i^{\mathrm{Th}}/K_i^{\mathrm{Pa}}$ and $g_{ca,op}^{\mathrm{Pa}} := \sigma_{ca}^{\mathrm{Pa}}/\sigma_{op}^{\mathrm{Pa}}$ and then give their scavenging coefficients σ_i^j in their equations 5a–6b, which we repeat here:

$$\sigma_{POC}^{Pa} = \sigma_0 \cdot f_{POC} \tag{B1}$$

$$\sigma_{ca}^{Pa} = \sigma_0 \cdot f_{ca} \tag{B2}$$

$$\sigma_{op}^{Pa} = \sigma_0 \cdot f_{ca} \cdot g_{ca,op}^{Pa} = \sigma_{ca}^{Pa} \cdot g_{ca,op}^{Pa} \tag{B3}$$

$$\sigma_{litho}^{Pa} = \sigma_0 \cdot f_{litho} \tag{B4}$$

$$\sigma_{POC,ca,litho}^{Th} = \sigma_0 \cdot 1 \tag{B5}$$

$$\sigma_{op}^{Th} = \sigma_0 \cdot f_{ca} \cdot g_{ca,op}^{Pa} \cdot f_{op}^{-1} = \sigma_{op}^{Pa} \cdot f_{op}^{-1}, \tag{B6}$$

where they used $\sigma_0 = 1\ \mathrm{m}^2/\mathrm{mol}, f_{POC} = 1, f_{op} = 1$ and $f_{ca} = 10, f_{litho} = 10, g_{ca,op}^{\mathrm{Pa}} = 1$ (given in their Table A2). Our proposed correct formulation of their Equations 5a–6b is:

$$\sigma_{POC}^{Pa} = \sigma_0 \cdot f_{POC}^{-1} \tag{B7}$$

$$\sigma_{ca}^{Pa} = \sigma_0 \cdot f_{ca}^{-1} \tag{B8}$$

$$\sigma_{op}^{Pa} = \sigma_0 \cdot f_{ca}^{-1} \cdot \left(g_{ca,op}^{Pa}\right)^{-1} = \sigma_{ca}^{Pa} \cdot \left(g_{ca,op}^{Pa}\right)^{-1} \tag{B9}$$

$$\sigma_{litho}^{Pa} = \sigma_0 \cdot f_{litho}^{-1} \tag{B10}$$

$$\sigma_{POC,ca,litho}^{Th} = \sigma_0 \cdot 1 \tag{B11}$$

$$\sigma_{op}^{Th} = \sigma_0 \cdot f_{ca}^{-1} \cdot \left(g_{ca,op}^{Pa}\right)^{-1} \cdot f_{op} = \sigma_{op}^{Pa} \cdot f_{op}, \tag{B12}$$

The latter formulation gives the σ_i^j values as in Table 3, whereas the original equations give $\sigma_{ca}^{\mathrm{Pa}} = 10 \cdot \sigma_{ca}^{\mathrm{Th}}$, which contradicts the notion that ^{231}Pa is generally less particle-reactive than ^{230}Th. Inspection of the code of the Bern3D model version 1.0—the version applied by Rempfer et al. (2017) - shows that these authors used the correct values of σ_i^j.

In addition, the caption of figure 2 published by Rempfer et al. (2017) mentions "along GEOTRACES transect GA03 (Hayes, Anderson, Fleisher, Vivancos, et al., 2015)." Based on the map in their figure A4, this should rather be: "along GEOTRACES transect GA03 (Hayes, Anderson, Fleisher, Vivancos, et al., 2015) until the crossing with GA02, and then continuing northwards on GA02."

Appendix C: Additional Figures and Tables

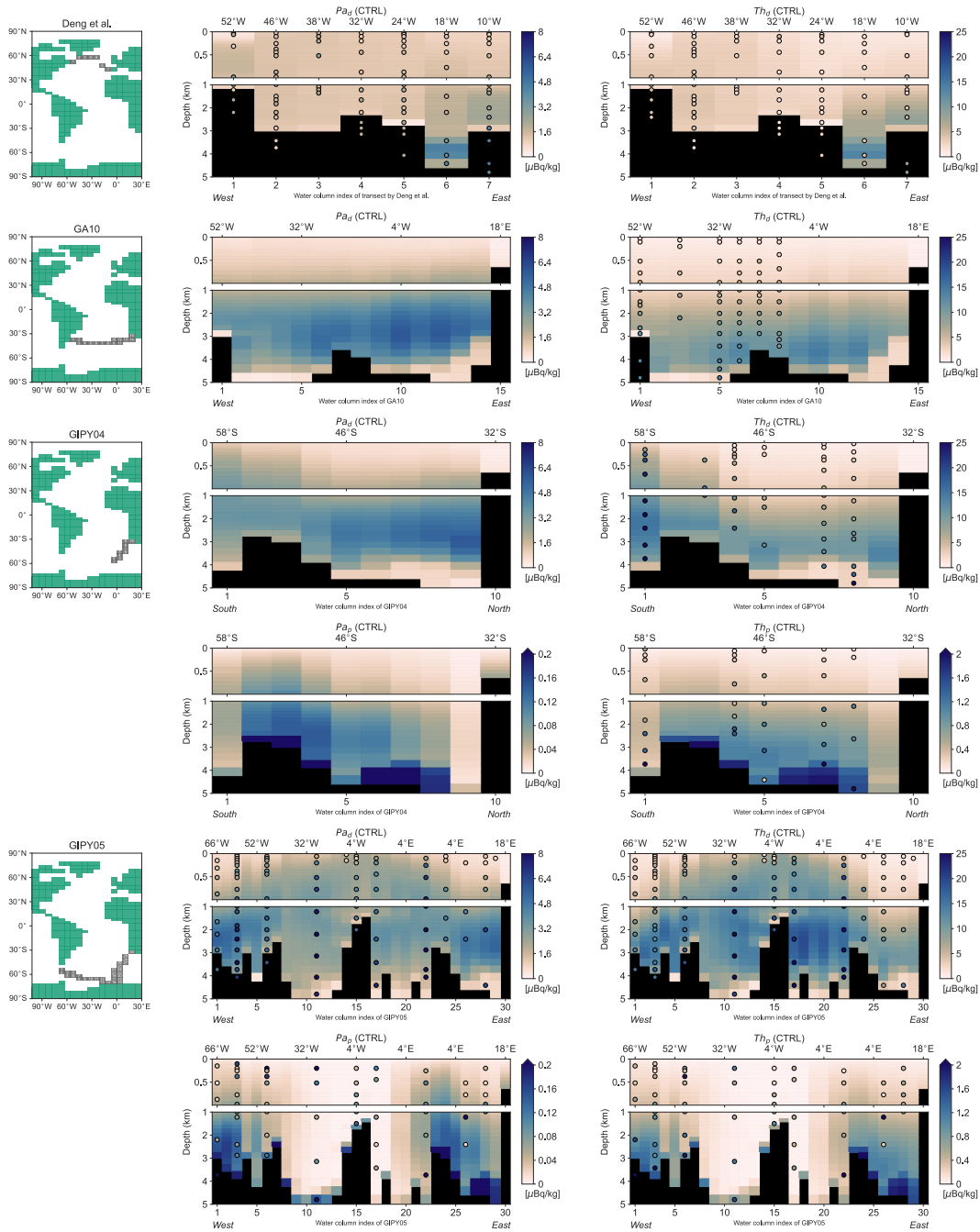

Figure C1. CTRL model output (background) with seawater observations (circles) along more transects in the Atlantic and the Atlantic sector of the Southern Ocean for $^{231}Pa_d$, $^{230}Th_d$, $^{231}Pa_p$, and $^{230}Th_p$ (where available). Data references in Section 2.3. Numbering on the transect maps (left) defines the order of plotting and corresponds to the water column indices on the *x*-axis of that transect. Seawater data circles are plotted centered in the nearest model grid cell box. If a grid cell contains multiple seawater observations, an uncertainty-weighted average is taken.

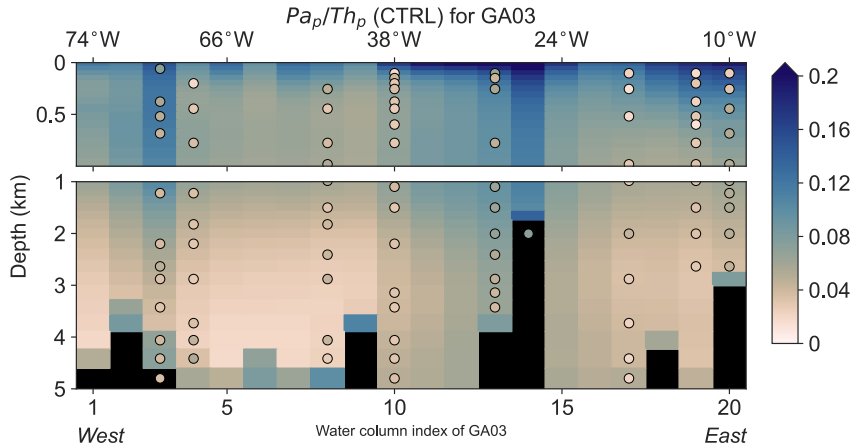

Figure C2. CTRL model output (background) with seawater observations (circles) for the $^{231}Pa_p/^{230}Th_p$ ratio along the east-west Atlantic transect GA03. See Figure 3d for the trajectory map of GA03; see Figures 5e and 5f for the separate $^{231}Pa_p$ and $^{230}Th_p$ concentrations.

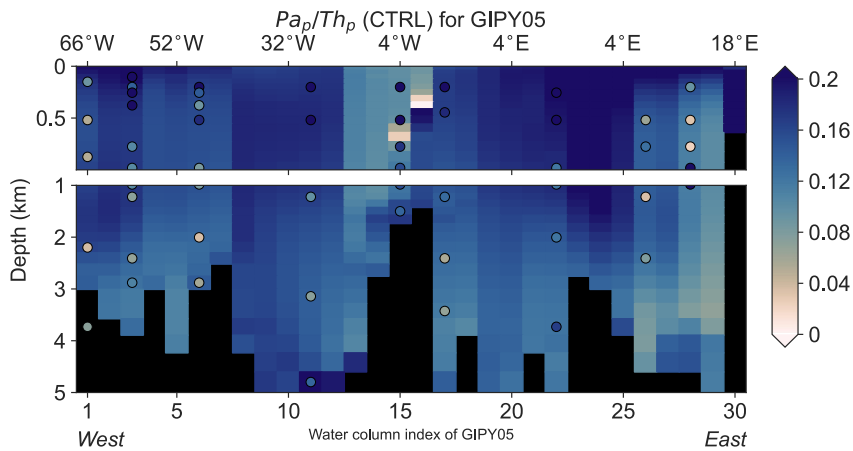

Figure C3. CTRL model output (background) with seawater observations (circles) for the $^{231}Pa_p/^{230}Th_p$ ratio along the GIPY05 transect in the Atlantic sector of the Southern Ocean. See Figure C1 for the trajectory map of GIPY05 and the separate $^{231}Pa_p$ and $^{230}Th_p$ concentrations.

10.1029/2024PA004869

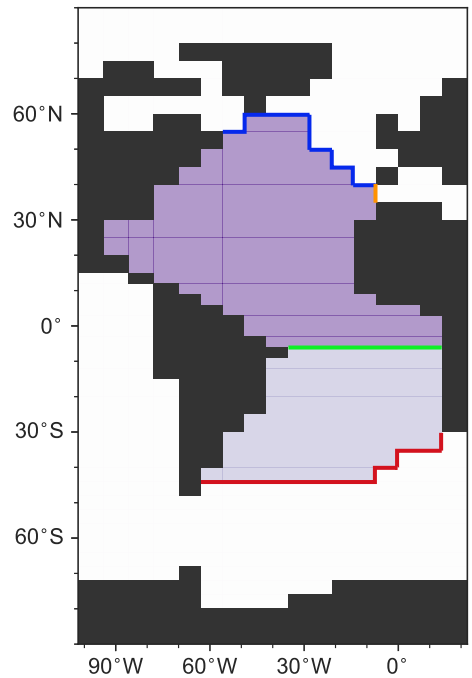

Figure C4. Definition of North Atlantic and South Atlantic sub-basins as used for budget calculations: confined by GEOVIDE (blue), WOCE A07 (green) and WOCE A11 (red), transferred to the Bern3D model grid. The boundary with the Mediterranean Sea (MED; orange) is also used in the budget calculation.

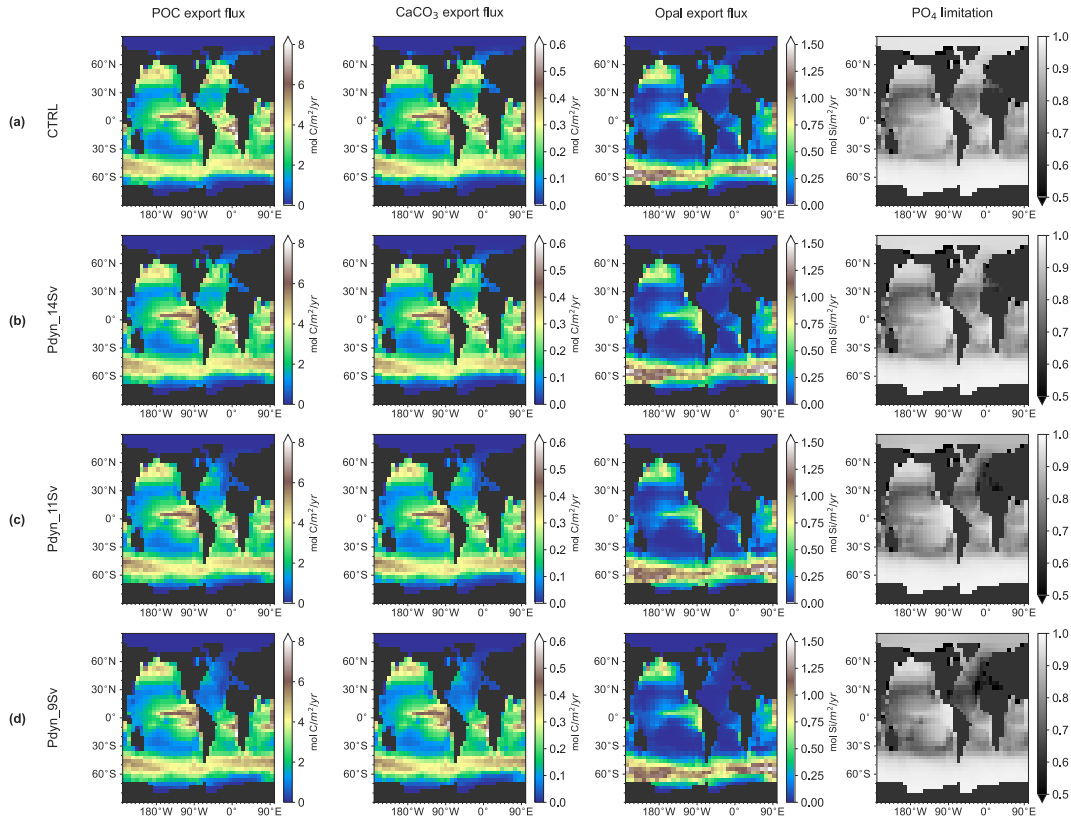

Figure C5. Export production of particulate organic carbon (POC), calcium carbonate and opal, induced by different ocean circulation states corresponding to Atlantic Meridional Overturning Circulation (AMOC) strengths of (a) the CTRL run (CTRL = Pdyn_18Sv; equal to Figures 2a–2c) and for runs with a weakened AMOC of (b) 14 Sv, (c) 11 Sv, and (d) 9 Sv. Also plotted is the limiting factor of surface PO_4 concentrations on particle production (right-most column; 1 is no limitation, 0 is total limitation). Patterns of POC and $CaCO_3$ are almost identical, because $CaCO_3$ production is set proportional to POC production in most regions of the Bern3D model (a strong assumption).

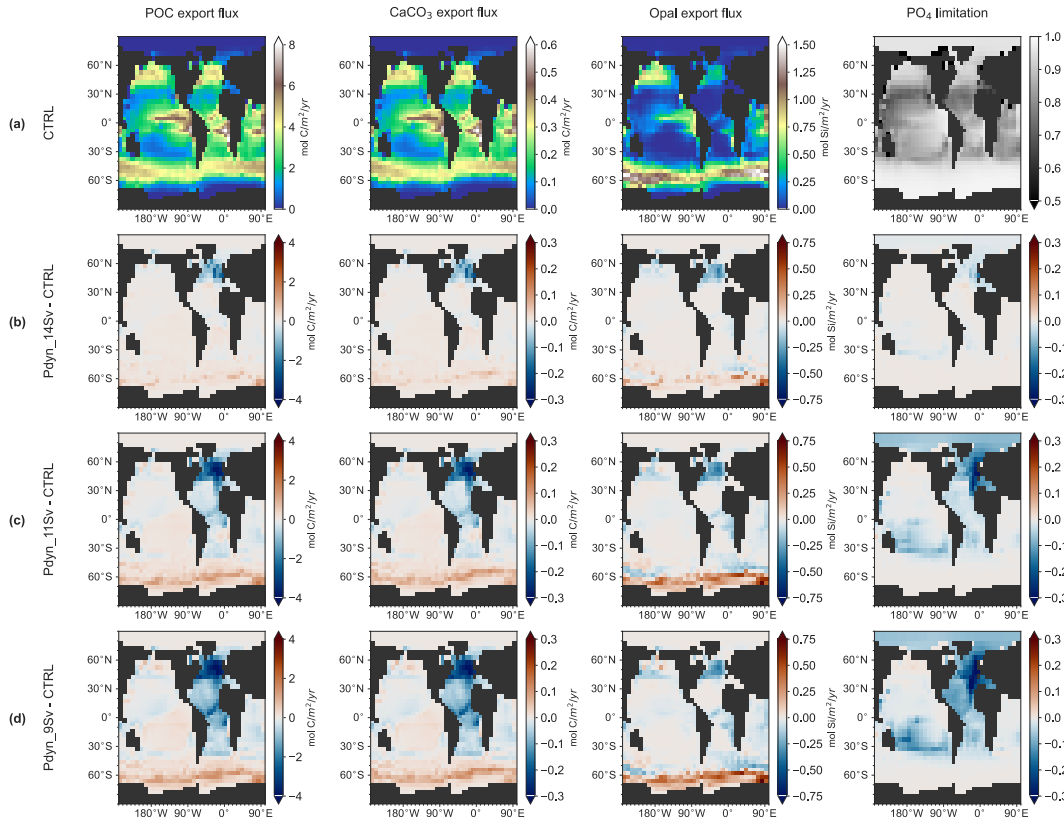

Figure C6. Export production: as Figure C5, but now the anomalies with respect to row (a) are shown.

Table C1
Additional Model Runs Used in Figure 9, in Addition to Runs in Table 4 of the Main Text

Runname	AMOC	Forcing[a]	Biological particles[b]	Description
P/2_18Sv	17.8 Sv	–	×0.5	Half of CTRL particles
P/2_14Sv	13.9 Sv	0.10	×0.5	~14 Sv AMOC; particles fixed to 0.5 ×CTRL
P/2_11Sv	11.2 Sv	0.15	×0.5	~11 Sv AMOC; particles fixed to 0.5 ×CTRL
P/2_9Sv	8.6 Sv	0.20	×0.5	etc.
Px2_18Sv	17.8 Sv	–	×2	Double of CTRL particles
Px2_14Sv	13.9 Sv	0.10	×2	~14 Sv AMOC; particles fixed to 2 ×CTRL
Px2_11Sv	11.2 Sv	0.15	×2	etc.
Px2_9Sv	8.6 Sv	0.20	×2	
Px3_18Sv	17.8 Sv	–	×3	Triple of CTRL particles
Px3_14Sv	13.9 Sv	0.10	×3	
Px3_11Sv	11.2 Sv	0.15	×3	
Px3_9Sv	8.6 Sv	0.20	×3	
Px5_18Sv	17.8 Sv	–	×5	CTRL particles times 5
Px5_14Sv	13.9 Sv	0.10	×5	
Px5_11Sv	11.2 Sv	0.15	×5	
Px5_9Sv	8.6 Sv	0.20	×5	

Note. All simulations were run into steady state for 5,000 years. All runs have the same parameter settings, dust and nepheloid particles as CTRL, unless indicated otherwise. Biological particles consist of POC, $CaCO_3$ and opal. [a]Freshwater forcing [Sv] in the North Atlantic between 45° and 70°N. [b]All runs here have biological particles fixed to (yearly avg.) particles from CTRL × a factor.

Data Availability Statement

We made use of seawater ^{231}Pa and ^{230}Th measurements from Deng et al. (2018), Ng et al. (2020), Pavia et al. (2020), and from the GEOTRACES Intermediate Data Product Group (2021). The GEOTRACES 2021 Intermediate Data Product (IDP2021) represents an international collaboration and is endorsed by the Scientific Committee on Oceanic Research (SCOR). The many researchers and funding agencies responsible for the collection of data and quality control are thanked for their contributions to the IDP2021. We used previously published sedimentary ^{231}Pa/^{230}Th-records from Anderson et al. (2014), Bradtmiller et al. (2007, 2014), Burckel et al. (2015), Gherardi et al. (2005, 2009), Hall et al. (2006), Hickey (2010), Hoffmann et al. (2018), Lippold et al. (2011, 2012a), Lippold, Mulitza, et al. (2012), Lippold et al. (2016), Lippold et al. (2019), McManus et al. (2004), Mulitza et al. (2017), Negre et al. (2010), Ng et al. (2018, 2020), Roberts et al. (2014), Süfke et al. (2019, 2020), and Waelbroeck et al. (2018). New sediment ^{231}Pa/^{230}Th measurements of this study are available at PANGAEA (Lippold et al., 2024). The Bern3D model is closed-source, but the output of model simulations used in this study is available in netCDF format on zenodo (Scheen et al., 2024). The output of the many tuning runs is not available, yet their $\left(w_s, k^j_{des}, \sigma^j_i\right)$ parameter settings and resulting MAEs can be found in the csv files of the same repository (Scheen et al., 2024). The code to analyze the model runs and to generate the figures is shared in another repository (Scheen et al., 2025) in well-documented python notebooks. We used python with a.o. the package cmcrameri for color maps (Crameri, 2023), xESMF for regridding (Zhuang et al., 2023) and plotting routines from Scheen (2020). In the case of questions or suspected bugs, please contact the corresponding author Jeemijn Scheen.

Acknowledgments

This research was supported by the Swiss National Science Foundation (Grants SNF 200020_172745 and 200020_200492, awarded to TFS) and the Deutsche Forschungsgemeinschaft (Grant LI1815/4, awarded to JL). FP was financially supported by the European Union's Horizon 2020 research and innovation program (Grant 101023443; project CliMoTran). We gratefully acknowledge Christoph C. Raible for helpful comments on an earlier version of the manuscript. We thank Janne Repschläger, Delia Oppo, Lars Max, Samuel Jaccard, and the ODP core repository in Bremen for providing sediment sample material. We thank Marcel Regelous for enabling the ICP-MS measurements at the GeoCenter Northern Bavaria, Erlangen. We thank Feifei Deng and Lise Missiaen for answering questions about their papers. We thank Alexey Mishonov, Mary Jo Richardson and Wilford Gardner for providing the data behind their figures (later published as Gardner et al. (2020)). Calculations were performed on UBELIX (https://www.id.unibe.ch/hpc), the HPC cluster at the University of Bern.

References

Abrantes, F. (2000). 200000 yr diatom records from Atlantic upwelling sites reveal maximum productivity during LGM and a shift in phytoplankton community structure at 185000 yr. *Earth and Planetary Science Letters*, *176*(1), 7–16. https://doi.org/10.1016/S0012-821X(99)00312-X

Anderson, R. F., Bacon, M. P., & Brewer, P. G. (1983). Removal of ^{230}Th and ^{231}Pa from the open ocean. *Earth and Planetary Science Letters*, *62*(1), 7–23. https://doi.org/10.1016/0012-821X(83)90067-5

Anderson, R. F., Barker, S., Fleisher, M., Gersonde, R., Goldstein, S. L., Kuhn, G., et al. (2014). Biological response to millennial variability of dust and nutrient supply in the Subantarctic South Atlantic Ocean. *Philosophical Transactions of the Royal Society A: Mathematical, Physical and Engineering Sciences*, *372*(2019), 20130054. https://doi.org/10.1098/rsta.2013.0054

Anderson, R. F., Cheng, H., Edwards, R. L., Fleisher, M. Q., Hayes, C. T., Huang, K.-F., et al. (2016). How well can we quantify dust deposition to the ocean? *Philosophical Transactions of the Royal Society A: Mathematical, Physical and Engineering Sciences*, *374*(2081), 20150285. https://doi.org/10.1098/rsta.2015.0285

Arsouze, T., Dutay, J.-C., Lacan, F., & Jeandel, C. (2009). Reconstructing the Nd oceanic cycle using a coupled dynamical–biogeochemical model. *Biogeosciences*, *6*(12), 2829–2846. https://doi.org/10.5194/bg-6-2829-2009

Bacon, M. P., & Anderson, R. F. (1982). Distribution of thorium isotopes between dissolved and particulate forms in the deep sea. *Journal of Geophysical Research*, *87*(C3), 2045–2056. https://doi.org/10.1029/JC087iC03p02045

Böhm, E., Lippold, J., Gutjahr, M., Frank, M., Blaser, P., Antz, B., et al. (2015). Strong and deep Atlantic meridional overturning circulation during the last glacial cycle. *Nature*, *517*(7532), 73–76. https://doi.org/10.1038/nature14059

Bourne, M. D., Thomas, A. L., Mac Niocaill, C., & Henderson, G. M. (2012). Improved determination of marine sedimentation rates using ^{230}Th$_{xs}$. *Geochemistry, Geophysics, Geosystems*, *13*(9), Q09017. https://doi.org/10.1029/2012GC004295

Bradtmiller, L. I., Anderson, R. F., Fleisher, M. Q., & Burckle, L. H. (2007). Opal burial in the equatorial Atlantic Ocean over the last 30 ka: Implications for glacial-interglacial changes in the ocean silicon cycle. *Paleoceanography*, *22*(4), PA4216. https://doi.org/10.1029/2007PA001443

Bradtmiller, L. I., McManus, J. F., & Robinson, L. F. (2014). ^{231}Pa/^{230}Th evidence for a weakened but persistent Atlantic meridional overturning circulation during Heinrich Stadial 1. *Nature Communications*, *5*(1), 5817. https://doi.org/10.1038/ncomms6817

Burckel, P., Waelbroeck, C., Gherardi, J. M., Pichat, S., Arz, H., Lippold, J., et al. (2015). Atlantic Ocean circulation changes preceded millennial tropical South America rainfall events during the last glacial. *Geophysical Research Letters*, *42*(2), 411–418. https://doi.org/10.1002/2014GL062512

Burckel, P., Waelbroeck, C., Luo, Y., Roche, D. M., Pichat, S., Jaccard, S. L., et al. (2016). Changes in the geometry and strength of the Atlantic meridional overturning circulation during the last glacial (20–50 ka). *Climate of the Past*, *12*(11), 2061–2075. https://doi.org/10.5194/cp-12-2061-2016

Burke, A., Marchal, O., Bradtmiller, L. I., McManus, J. F., & François, R. (2011). Application of an inverse method to interpret ^{231}Pa/^{230}Th observations from marine sediments. *Paleoceanography*, *26*(1), PA1212. https://doi.org/10.1029/2010PA002022

Carroll, D., & Starkey, H. C. (1958). Effect of sea-water on clay minerals. *Clays and Clay Minerals*, *7*, 80–101. https://doi.org/10.1346/CCMN.1958.0070103

Chase, Z., Anderson, R. F., Fleisher, M. Q., & Kubik, P. W. (2002). The influence of particle composition and particle flux on scavenging of Th, Pa and Be in the ocean. *Earth and Planetary Science Letters*, *204*(1–2), 215–229. https://doi.org/10.1016/S0012-821X(02)00984-6

Chen, J. H., Lawrence Edwards, R., & Wasserburg, G. J. (1986). ^{238}U, ^{234}U and ^{232}Th in seawater. *Earth and Planetary Science Letters*, *80*(3–4), 241–251. https://doi.org/10.1016/0012-821X(86)90108-1

Chen, S.-Y. S., Marchal, O., Lerner, P. E., McCorkle, D. C., & Rutgers van der Loeff, M. M. (2021). On the cycling of ^{231}Pa and ^{230}Th in benthic nepheloid layers. *Deep Sea Research Part I: Oceanographic Research Papers*, *177*, 103627. https://doi.org/10.1016/j.dsr.2021.103627

Crameri, F. (2023). Scientific colour maps [Software]. *Zenodo*. https://doi.org/10.5281/zenodo.8035877

Deng, F., Henderson, G. M., Castrillejo, M., Perez, F. F., & Steinfeldt, R. (2018). Evolution of ^{231}Pa and ^{230}Th in overflow waters of the North Atlantic. *Biogeosciences*, *15*(23), 7299–7313. https://doi.org/10.5194/bg-15-7299-2018

Deng, F., Thomas, A. L., Rijkenberg, M. J., & Henderson, G. M. (2014). Controls on seawater ^{231}Pa, ^{230}Th and ^{232}Th concentrations along the flow paths of deep waters in the Southwest Atlantic. *Earth and Planetary Science Letters*, *390*, 93–102. https://doi.org/10.1016/j.epsl.2013.12.038

Dinauer, A., Laufkötter, C., Doney, S. C., & Joos, F. (2022). What controls the large-scale efficiency of carbon transfer through the ocean's mesopelagic zone? Insights from a new, mechanistic model (MSPACMAM). *Global Biogeochemical Cycles*, *36*(10), e2021GB007131. https://doi.org/10.1029/2021GB007131

Dutay, J.-C., Lacan, F., Roy-Barman, M., & Bopp, L. (2009). Influence of particle size and type on ^{231}Pa and ^{230}Th simulation with a global coupled biogeochemical-ocean general circulation model: A first approach. *Geochemistry, Geophysics, Geosystems*, *10*(1), Q01011. https://doi.org/10.1029/2008GC002291

Edwards, N. R., Willmott, A. J., & Killworth, P. D. (1998). On the role of topography and wind stress on the stability of the thermohaline circulation. *Journal of Physical Oceanography*, *28*(5), 756–778. https://doi.org/10.1175/1520-0485(1998)028⟨0756:OTROTA⟩2.0.CO;2

Fietzke, J., Bollhöfer, A., Frank, N., & Mangini, A. (1999). Protactinium determination in manganese crust VA13/2 by thermal ionization mass spectrometry (TIMS). *Nuclear Instruments and Methods in Physics Research Section B: Beam Interactions with Materials and Atoms*, *149*(3), 353–360. https://doi.org/10.1016/S0168-583X(98)00912-4

Gardner, W. D., Mishonov, A. V., & Richardson, M. J. (2020). Global transmissometer database v3 [Dataset]. *Ocean Data View*. Retrieved from https://odv.awi.de/data/ocean/global-transmissometer-database/

Gardner, W. D., Richardson, M. J., & Mishonov, A. V. (2018). Global assessment of benthic nepheloid layers and linkage with upper ocean dynamics. *Earth and Planetary Science Letters*, *482*, 126–134. https://doi.org/10.1016/j.epsl.2017.11.008

Gardner, W. D., Richardson, M. J., Mishonov, A. V., & Biscaye, P. E. (2018). Global comparison of benthic nepheloid layers based on 52 years of nephelometer and transmissometer measurements. *Progress in Oceanography*, *168*, 100–111. https://doi.org/10.1016/j.pocean.2018.09.008

Gebbie, G. (2014). How much did Glacial North Atlantic Water shoal? *Paleoceanography*, *29*(3), 190–209. https://doi.org/10.1002/2013PA002557

Geibert, W., & Usbeck, R. (2004). Adsorption of thorium and protactinium onto different particle types: Experimental findings. *Geochimica et Cosmochimica Acta*, *68*(7), 1489–1501. https://doi.org/10.1016/j.gca.2003.10.011

GEOTRACES Intermediate Data Product Group. (2021). The GEOTRACES Intermediate Data Product 2021 (IDP2021) [Dataset]. *NERC EDS British Oceanographic Data Centre NOC*. https://doi.org/10.5285/cf2d9ba9-d51d-3b7c-e053-8486abc0f5fd

Gherardi, J.-M., Labeyrie, L., McManus, J., François, R., Skinner, L., & Cortijo, E. (2005). Evidence from the Northeastern Atlantic basin for variability in the rate of the meridional overturning circulation through the last deglaciation. *Earth and Planetary Science Letters*, *240*(3–4), 710–723. https://doi.org/10.1016/j.epsl.2005.09.061

Gherardi, J.-M., Labeyrie, L., Nave, S., François, R., McManus, J. F., & Cortijo, E. (2009). Glacial-interglacial circulation changes inferred from ^{231}Pa/^{230}Th sedimentary record in the North Atlantic region. *Paleoceanography*, *24*(2), PA2204. https://doi.org/10.1029/2008PA001696

Gu, S., & Liu, Z. (2017). ^{231}Pa and ^{230}Th in the ocean model of the Community Earth System Model (CESM1.3). *Geoscientific Model Development*, *10*(12), 4723–4742. https://doi.org/10.5194/gmd-10-4723-2017

Gu, S., Liu, Z., Jahn, A., Rempfer, J., Zhang, J., & Joos, F. (2019). Modeling neodymium isotopes in the ocean component of the Community Earth System Model (CESM1). *Journal of Advances in Modeling Earth Systems*, *11*(3), 624–640. https://doi.org/10.1029/2018MS001538

Gu, S., Liu, Z., Oppo, D. W., Lynch-Stieglitz, J., Jahn, A., Zhang, J., & Wu, L. (2020). Assessing the potential capability of reconstructing glacial Atlantic water masses and AMOC using multiple proxies in CESM. *Earth and Planetary Science Letters*, *541*, 116294. https://doi.org/10.1016/j.epsl.2020.116294

Hall, I. R., Moran, S. B., Zahn, R., Knutz, P. C., Shen, C.-C., & Edwards, R. L. (2006). Accelerated drawdown of meridional overturning in the late-glacial Atlantic triggered by transient pre-H event freshwater perturbation. *Geophysical Research Letters*, *33*(16), L16616. https://doi.org/10.1029/2006GL026239

Hayes, C. T., Anderson, R. F., Fleisher, M. Q., Huang, K.-F., Robinson, L. F., Lu, Y., et al. (2015). ^{230}Th and ^{231}Pa on GEOTRACES GA03, the U. S. GEOTRACES North Atlantic transect, and implications for modern and paleoceanographic chemical fluxes. *Deep Sea Research Part II: Topical Studies in Oceanography*, *116*, 29–41. https://doi.org/10.1016/j.dsr2.2014.07.007

Hayes, C. T., Anderson, R. F., Fleisher, M. Q., Vivancos, S. M., Lam, P. J., Ohnemus, D. C., et al. (2015). Intensity of Th and Pa scavenging partitioned by particle chemistry in the North Atlantic Ocean. *Marine Chemistry*, *170*, 49–60. https://doi.org/10.1016/j.marchem.2015.01.006

Hayes, C. T., Anderson, R. F., Jaccard, S. L., François, R., Fleisher, M. Q., Soon, M., & Gersonde, R. (2013). A new perspective on boundary scavenging in the North Pacific Ocean. *Earth and Planetary Science Letters*, *369–370*, 86–97. https://doi.org/10.1016/j.epsl.2013.03.008

Hayes, C. T., Rosen, J., McGee, D., & Boyle, E. A. (2017). Thorium distributions in high- and low-dust regions and the significance for iron supply. *Global Biogeochemical Cycles*, *31*(2), 328–347. https://doi.org/10.1002/2016GB005511

Heinze, C., Gehlen, M., & Land, C. (2006). On the potential of ^{230}Th, ^{231}Pa, and ^{10}Be for marine rain ratio determinations: A modeling study. *Global Biogeochemical Cycles*, *20*(2), GB2018. https://doi.org/10.1029/2005GB002595

Henderson, G. M., Heinze, C., Anderson, R. F., & Winguth, A. M. (1999). Global distribution of the ^{230}Th flux to ocean sediments constrained by GCM modelling. *Deep Sea Research Part I: Oceanographic Research Papers*, *46*(11), 1861–1893. https://doi.org/10.1016/S0967-0637(99)00030-8

Henry, L. G., McManus, J. F., Curry, W. B., Roberts, N. L., Piotrowski, A. M., & Keigwin, L. D. (2016). North Atlantic ocean circulation and abrupt climate change during the last glaciation. *Science*, *353*(6298), 470–474. https://doi.org/10.1126/science.aaf5529

Hickey, B. (2010). *Reconstructing past flow rates of Southern component water masses using sedimentary ^{231}Pa/^{230}Th* [Doctoral dissertation]. University of Oxford.

Hoffmann, S. S., McManus, J. F., & Swank, E. (2018). Evidence for stable Holocene basin-scale overturning circulation despite variable currents along the deep western boundary of the North Atlantic Ocean. *Geophysical Research Letters*, *45*(24), 13427–13436. https://doi.org/10.1029/2018GL080187

Jeltsch-Thömmes, A., Battaglia, G., Cartapanis, O., Jaccard, S. L., & Joos, F. (2019). Low terrestrial carbon storage at the Last Glacial Maximum: Constraints from multi-proxy data. *Climate of the Past*, *15*(2), 849–879. https://doi.org/10.5194/cp-15-849-2019

Kalnay, E., Kanamitsu, M., Kistler, R., Collins, W., Deaven, D., Gandin, L., et al. (1996). The NCEP/NCAR 40-year reanalysis project. *Bulletin of the American Meteorological Society*, *77*(3), 437–472. https://doi.org/10.1175/1520-0477(1996)077⟨0437:TNYRP⟩2.0.CO;2

Khatiwala, S. (2023). Fast spin-up of geochemical tracers in ocean circulation and climate models. *Journal of Advances in Modeling Earth Systems*, *15*(2), e2022MS003447. https://doi.org/10.1029/2022MS003447

Kretschmer, S., Geibert, W., Rutgers van der Loeff, M. M., Schnabel, C., Xu, S., & Mollenhauer, G. (2011). Fractionation of ^{230}Th, ^{231}Pa, and ^{10}Be induced by particle size and composition within an opal-rich sediment of the Atlantic Southern Ocean. *Geochimica et Cosmochimica Acta*, *75*(22), 6971–6987. https://doi.org/10.1016/j.gca.2011.09.012

Lerner, P., Marchal, O., Lam, P. J., Gardner, W., Richardson, M. J., & Mishonov, A. (2020). A model study of the relative influences of scavenging and circulation on ^{230}Th and ^{231}Pa in the western North Atlantic. *Deep Sea Research Part I: Oceanographic Research Papers*, *155*, 103–159. https://doi.org/10.1016/j.dsr.2019.103159

Levier, M., Roy-Barman, M., Foliot, L., Dapoigny, A., & Lacan, F. (2022). Distribution of Pa in the Atlantic sector of the Southern Ocean: Tracking scavenging during water mass mixing along neutral density surfaces. *Deep Sea Research Part I: Oceanographic Research Papers*, *194*, 103951. https://doi.org/10.1016/j.dsr.2022.103951

Li, S., Goldstein, S. L., & Raymo, M. E. (2021). Neogene continental denudation and the beryllium conundrum. *Proceedings of the National Academy of Sciences*, *118*(42), e2026456118. https://doi.org/10.1073/pnas.2026456118

Lippold, J., Gherardi, J.-M., & Luo, Y. (2011). Testing the ^{231}Pa/^{230}Th paleocirculation proxy: A data versus 2D model comparison. *Geophysical Research Letters*, *38*(20), L20603. https://doi.org/10.1029/2011GL049282

Lippold, J., Gutjahr, M., Blaser, P., Christner, E., de Carvalho Ferreira, M. L., Mulitza, S., et al. (2016). Deep water provenance and dynamics of the (de)glacial Atlantic meridional overturning circulation. *Earth and Planetary Science Letters*, *445*, 68–78. https://doi.org/10.1016/j.epsl.2016.04.013

Lippold, J., Luo, Y., François, R., Allen, S. E., Gherardi, J., Pichat, S., et al. (2012). Strength and geometry of the glacial Atlantic Meridional Overturning Circulation. *Nature Geoscience*, *5*(11), 813–816. https://doi.org/10.1038/ngeo1608

Lippold, J., Mulitza, S., Mollenhauer, G., Weyer, S., Heslop, D., & Christl, M. (2012). Boundary scavenging at the East Atlantic margin does not negate use of ^{231}Pa/^{230}Th to trace Atlantic overturning. *Earth and Planetary Science Letters*, *333–334*, 317–331. https://doi.org/10.1016/j.epsl.2012.04.005

Lippold, J., Pöppelmeier, F., Süfke, F., Gutjahr, M., Goepfert, T. J., Blaser, P., et al. (2019). Constraining the variability of the Atlantic meridional overturning circulation during the Holocene. *Geophysical Research Letters*, *46*(20), 11338–11346. https://doi.org/10.1029/2019GL084988

Lippold, J., Scheen, J., Pöppelmeier, F., Süfke, F., Stocker, T. F., & Regelous, M. (2024). ^{231}Pa/^{230}Th (Pa/Th) and related radioisotope concentrations from eleven Atlantic sediment cores for the Holocene [Dataset]. *PANGAEA*. https://doi.org/10.1594/PANGAEA.971789

Luo, S., & Ku, T.-L. (1999). Oceanic ^{231}Pa/^{230}Th ratio influenced by particle composition and remineralization. *Earth and Planetary Science Letters*, *167*(3), 183–195. https://doi.org/10.1016/S0012-821X(99)00035-7

Luo, S., & Ku, T.-L. (2004a). On the importance of opal, carbonate, and lithogenic clays in scavenging and fractionating ^{230}Th, ^{231}Pa and ^{10}Be in the ocean. *Earth and Planetary Science Letters*, *220*(1–2), 201–211. https://doi.org/10.1016/S0012-821X(04)00027-5

Luo, Y., François, R., & Allen, S. E. (2010). Sediment ^{231}Pa/^{230}Th as a recorder of the rate of the Atlantic meridional overturning circulation: Insights from a 2-D model. *Ocean Science*, *6*(1), 381–400. https://doi.org/10.5194/os-6-381-2010

Luo, Y., Lippold, J., Allen, S. E., Tjiputra, J., Jaccard, S. L., & François, R. (2021). The influence of deep water circulation on the distribution of ^{231}Pa and ^{230}Th in the Pacific Ocean. *Earth and Planetary Science Letters*, *554*, 116674. https://doi.org/10.1016/j.epsl.2020.116674

Lynch-Stieglitz, J. (2017). The Atlantic Meridional Overturning Circulation and abrupt climate change. *Annual Review of Marine Science*, *9*(1), 83–104. https://doi.org/10.1146/annurev-marine-010816-060415

Lynch-Stieglitz, J., Adkins, J. F., Curry, W. B., Dokken, T., Hall, I. R., Herguera, J. C., et al. (2007). Atlantic Meridional Overturning Circulation during the Last Glacial Maximum. *Science*, *316*(5821), 66–69. https://doi.org/10.1126/science.1137127

Mahowald, N. M., Muhs, D. R., Levis, S., Rasch, P. J., Yoshioka, M., Zender, C. S., & Luo, C. (2006). Change in atmospheric mineral aerosols in response to climate: Last glacial period, preindustrial, modern, and doubled carbon dioxide climates. *Journal of Geophysical Research*, *111*(10), D10202. https://doi.org/10.1029/2005JD006653

Marchal, O., François, R., & Scholten, J. (2007). Contribution of 230Th measurements to the estimation of the abyssal circulation. *Deep Sea Research Part I: Oceanographic Research Papers*, *54*(4), 557–585. https://doi.org/10.1016/j.dsr.2007.01.002

Marchal, O., François, R., Stocker, T. F., & Joos, F. (2000). Ocean thermohaline circulation and sedimentary ^{231}Pa/^{230}Th ratio. *Paleoceanography*, *15*(6), 625–641. https://doi.org/10.1029/2000PA000496

Martin, J. H., Knauer, G. A., Karl, D. M., & Broenkow, W. W. (1987). VERTEX: Carbon cycling in the northeast Pacific. *Deep Sea Research Part A. Oceanographic Research Papers*, *34*(2), 267–285. https://doi.org/10.1016/0198-0149(87)90086-0

McManus, J. F., François, R., Gherardi, J.-M., Keigwin, L. D., & Brown-Leger, S. (2004). Collapse and rapid resumption of Atlantic meridional circulation linked to deglacial climate changes. *Nature*, *428*(6985), 834–837. https://doi.org/10.1038/nature02494

Missiaen, L., Bouttes, N., Roche, D. M., Dutay, J.-C., Quiquet, A., Waelbroeck, C., et al. (2020). Carbon isotopes and Pa/Th response to forced circulation changes: A model perspective. *Climate of the Past*, *16*(3), 867–883. https://doi.org/10.5194/cp-16-867-2020

Missiaen, L., Menviel, L. C., Meissner, K. J., Roche, D. M., Dutay, J.-C., Bouttes, N., et al. (2020). Modelling the impact of biogenic particle flux intensity and composition on sedimentary Pa/Th. *Quaternary Science Reviews*, *240*, 106394. https://doi.org/10.1016/j.quascirev.2020.106394

Mulitza, S., Chiessi, C. M., Schefuß, E., Lippold, J., Wichmann, D., Antz, B., et al. (2017). Synchronous and proportional deglacial changes in Atlantic meridional overturning and northeast Brazilian precipitation. *Paleoceanography*, *32*(6), 622–633. https://doi.org/10.1002/2017PA003084

Müller, S. A., Joos, F., Edwards, N. R., & Stocker, T. F. (2006). Water mass distribution and ventilation time scales in a cost-efficient, three-dimensional ocean model. *Journal of Climate*, *19*(21), 5479–5499. https://doi.org/10.1175/JCLI3911.1

Negre, C., Zahn, R., Thomas, A. L., Masqué, P., Henderson, G. M., Martínez-Méndez, G., et al. (2010). Reversed flow of Atlantic deep water during the Last Glacial Maximum. *Nature*, *468*(7320), 84–88. https://doi.org/10.1038/nature09508

Ng, H. C., Robinson, L. F., McManus, J. F., Mohamed, K. J., Jacobel, A. W., Ivanovic, R. F., et al. (2018). Coherent deglacial changes in western Atlantic Ocean circulation. *Nature Communications*, *9*(1), 2947. https://doi.org/10.1038/s41467-018-05312-3

Ng, H. C., Robinson, L. F., Rowland, G. H., Chen, S. S., & McManus, J. F. (2020). Coupled analysis of seawater and sedimentary ^{231}Pa/^{230}Th in the tropical Atlantic. *Marine Chemistry*, *227*, 103894. https://doi.org/10.1016/j.marchem.2020.103894

Ni, Q., Zhai, X., LaCasce, J. H., Chen, D., & Marshall, D. P. (2023). Full-depth eddy kinetic energy in the global ocean estimated from altimeter and argo observations. *Geophysical Research Letters*, *50*(15), e2023GL103114. https://doi.org/10.1029/2023GL103114

Nielsen, S. B., Jochum, M., Pedro, J. B., Eden, C., & Nuterman, R. (2019). Two-timescale carbon cycle response to an AMOC collapse. *Paleoceanography and Paleoclimatology*, *34*(4), 511–523. https://doi.org/10.1029/2018PA003481

Okubo, A., Obata, H., Gamo, T., & Yamada, M. (2012). ^{230}Th and ^{232}Th distributions in mid-latitudes of the North Pacific Ocean: Effect of bottom scavenging. *Earth and Planetary Science Letters*, *339–340*, 139–150. https://doi.org/10.1016/j.epsl.2012.05.012

Parekh, P., Joos, F., & Müller, S. A. (2008). A modeling assessment of the interplay between aeolian iron fluxes and iron-binding ligands in controlling carbon dioxide fluctuations during Antarctic warm events. *Paleoceanography*, *23*(4), PA4202. https://doi.org/10.1029/2007PA001531

Pavia, F. J., Anderson, R. F., Black, E. E., Kipp, L. E., Vivancos, S. M., Fleisher, M. Q., et al. (2019). Timescales of hydrothermal scavenging in the South Pacific Ocean from ^{234}Th, ^{230}Th, and ^{228}Th. *Earth and Planetary Science Letters*, *506*, 146–156. https://doi.org/10.1016/j.epsl.2018.10.038

Pavia, F. J., Anderson, R. F., Pinedo-Gonzalez, P., Fleisher, M. Q., Brzezinski, M. A., & Robinson, R. S. (2020). Isopycnal transport and scavenging of ^{230}Th and ^{231}Pa in the Pacific Southern Ocean. *Global Biogeochemical Cycles*, *34*(12), e2020GB006760. https://doi.org/10.1029/2020GB006760

Pöppelmeier, F., Gutjahr, M., Blaser, P., Schulz, H., Süfke, F., & Lippold, J. (2021). Stable Atlantic deep water mass sourcing on glacial-interglacial timescales. *Geophysical Research Letters*, *48*(15), e2021GL092722. https://doi.org/10.1029/2021GL092722

Regelous, M., Turner, S. P., Elliott, T. R., Rostami, K., & Hawkesworth, C. J. (2004). Measurement of femtogram quantities of protactinium in silicate rock samples by multicollector inductively coupled plasma mass spectrometry. *Analytical Chemistry*, *76*(13), 3584–3589. https://doi.org/10.1021/ac0303741

Rempfer, J., Stocker, T. F., Joos, F., Dutay, J.-C., & Siddall, M. (2011). Modelling Nd-isotopes with a coarse resolution ocean circulation model: Sensitivities to model parameters and source/sink distributions. *Geochimica et Cosmochimica Acta*, *75*(20), 5927–5950. https://doi.org/10.1016/j.gca.2011.07.044

Rempfer, J., Stocker, T. F., Joos, F., Lippold, J., & Jaccard, S. L. (2017). New insights into cycling of 231Pa and 230Th in the Atlantic Ocean. *Earth and Planetary Science Letters*, *468*, 27–37. https://doi.org/10.1016/j.epsl.2017.03.027

Repschläger, J., Zhao, N., Rand, D., Lisiecki, L., Muglia, J., Mulitza, S., et al. (2021). Active North Atlantic deepwater formation during Heinrich Stadial 1. *Quaternary Science Reviews*, *270*, 107145. https://doi.org/10.1016/j.quascirev.2021.107145

Ritz, S. P., Stocker, T. F., & Joos, F. (2011). A coupled dynamical ocean-energy balance atmosphere model for paleoclimate studies. *Journal of Climate*, *24*(2), 349–375. https://doi.org/10.1175/2010JCLI3351.1

Roberts, N. L., McManus, J. F., Piotrowski, A. M., & McCave, I. N. (2014). Advection and scavenging controls of Pa/Th in the northern NE Atlantic. *Paleoceanography*, *29*(6), 668–679. https://doi.org/10.1002/2014PA002633

Roth, R., Ritz, S. P., & Joos, F. (2014). Burial-nutrient feedbacks amplify the sensitivity of atmospheric carbon dioxide to changes in organic matter remineralisation. *Earth System Dynamics*, *5*(2), 321–343. https://doi.org/10.5194/esd-5-321-2014

Roy-Barman, M., Thil, F., Bordier, L., Dapoigny, A., Foliot, L., Ayrault, S., et al. (2019). Thorium isotopes in the Southeast Atlantic Ocean: Tracking scavenging during water mass mixing along neutral density surfaces. *Deep Sea Research Part I: Oceanographic Research Papers*, *149*, 103042. https://doi.org/10.1016/j.dsr.2019.05.002

Sarmiento, J. L., & Gruber, N. (2006). *Ocean biogeochemical dynamics*. Princeton University Press.

Sasaki, Y., Kobayashi, H., & Oka, A. (2022). Global simulation of dissolved ^{231}Pa and ^{230}Th in the ocean and the sedimentary ^{231}Pa/^{230}Th ratios with the ocean general circulation model COCO ver4.0. *Geoscientific Model Development*, *15*(5), 2013–2033. https://doi.org/10.5194/gmd-15-2013-2022

Scheen, J. (2020). jeemijn/lia: Effect of changing ocean circulation on deep ocean temperature in the last millennium: Code [Software]. *Zenodo. (v1.1.0)*. https://doi.org/10.5281/zenodo.4022947

Scheen, J., Mishonov, A. V., Richardson, M. J., & Gardner, W. D. (2025). Code for: "Promising regions for detecting the overturning circulation in Atlantic Pa/Th: A model-data comparison" [Software]. *Zenodo. (v2.0.2)*. https://doi.org/10.5281/zenodo.14858662

Scheen, J., Pöppelmeier, F., & Stocker, T. F. (2024). Simulation output data for: "Promising regions for detecting the overturning circulation in Atlantic Pa/Th: A model-data comparison" [Dataset]. *Zenodo. (v2.0.0)*. https://doi.org/10.5281/zenodo.14791063

Schmiedl, G., & Mackensen, A. (1997). Late Quaternary paleoproductivity and deep water circulation in the eastern South Atlantic Ocean: Evidence from benthic foraminifera. *Palaeogeography, Palaeoclimatology, Palaeoecology*, *130*(1), 43–80. https://doi.org/10.1016/S0031-0182(96)00137-X

Schmittner, A. (2005). Decline of the marine ecosystem caused by a reduction in the Atlantic overturning circulation. *Nature*, *434*(7033), 628–633. https://doi.org/10.1038/nature03476

Siddall, M., Henderson, G. M., Edwards, N. R., Frank, M., Müller, S. A., Stocker, T. F., & Joos, F. (2005). ^{231}Pa/^{230}Th fractionation by ocean transport, biogenic particle flux and particle type. *Earth and Planetary Science Letters*, *237*(1–2), 135–155. https://doi.org/10.1016/j.epsl.2005.05.031

Stocker, T. F., Timmermann, A., Renold, M., & Timm, O. (2007). Effects of salt compensation on the climate model response in simulations of large changes of the Atlantic Meridional Overturning Circulation. *Journal of Climate*, *20*(24), 5912–5928. https://doi.org/10.1175/2007JCLI1662.1

Süfke, F., Lippold, J., & Happel, S. (2018). Improved separation of Pa from Th and U in marine sediments with TK400 Resin. *Analytical Chemistry*, *90*(2), 1395–1401. https://doi.org/10.1021/acs.analchem.7b04723

Süfke, F., Pöppelmeier, F., Goepfert, T. J., Regelous, M., Koutsodendris, A., Blaser, P., et al. (2019). Constraints on the Northwestern Atlantic deep water circulation from ^{231}Pa/^{230}Th during the last 30,000 years. *Paleoceanography and Paleoclimatology*, *34*(12), 1945–1958. https://doi.org/10.1029/2019PA003737

Süfke, F., Schulz, H., Scheen, J., Szidat, S., Regelous, M., Blaser, P., et al. (2020). Inverse response of ^{231}Pa/^{230}Th to variations of the Atlantic meridional overturning circulation in the North Atlantic intermediate water. *Geo-Marine Letters*, *40*(1), 75–87. https://doi.org/10.1007/s00367-019-00634-7

Tschumi, T., Joos, F., & Parekh, P. (2008). How important are Southern Hemisphere wind changes for low glacial carbon dioxide? A model study. *Paleoceanography*, *23*(4), PA4208. https://doi.org/10.1029/2008PA001592

van Hulten, M., Dutay, J.-C., & Roy-Barman, M. (2018). A global scavenging and circulation ocean model of thorium-230 and protactinium-231 with improved particle dynamics (NEMO–ProThorP 0.1). *Geoscientific Model Development*, *11*(9), 3537–3556. https://doi.org/10.5194/gmd-11-3537-2018

Venchiarutti, C., van der Loeff, M. R., & Stimac, I. (2011). Scavenging of ^{231}Pa and thorium isotopes based on dissolved and size-fractionated particulate distributions at Drake Passage (ANTXXIV-3). *Deep Sea Research Part II: Topical Studies in Oceanography*, *58*(25–26), 2767–2784. https://doi.org/10.1016/j.dsr2.2010.10.040

Waelbroeck, C., Pichat, S., Böhm, E., Lougheed, B. C., Faranda, D., Vrac, M., et al. (2018). Relative timing of precipitation and ocean circulation changes in the western equatorial Atlantic over the last 45 kyr. *Climate of the Past*, *14*(9), 1315–1330. https://doi.org/10.5194/cp-14-1315-2018

Wollenburg, J. E., Knies, J., & Mackensen, A. (2004). High-resolution paleoproductivity fluctuations during the past 24 kyr as indicated by benthic foraminifera in the marginal Arctic Ocean. *Palaeogeography, Palaeoclimatology, Palaeoecology*, *204*(3), 209–238. https://doi.org/10.1016/S0031-0182(03)00726-0

Yu, E.-F., François, R., & Bacon, M. P. (1996). Similar rates of modern and last-glacial ocean thermohaline circulation inferred from radiochemical data. *Nature*, *379*(6567), 689–694. https://doi.org/10.1038/379689a0

Zhang, X., Yang, W., Qiu, Y., & Zheng, M. (2021). Adsorption of Th and Pa onto particles and the effect of organic compounds in natural seawater. *Journal of Oceanology and Limnology*, *39*(6), 2209–2219. https://doi.org/10.1007/s00343-021-0297-5

Zhuang, J., Dussin, R., Huard, D., Bourgault, P., Banihirwe, A., Raynaud, S., et al. (2023). pangeo-data/xesmf: v0.8.2 [Software]. *Zenodo*. https://doi.org/10.5281/zenodo.8356796

References From the Supporting Information

Blaauw, M., & Christen, J. A. (2011). Flexible paleoclimate age-depth models using an autoregressive gamma process. *Bayesian Analysis*, *6*(3), 457–474. https://doi.org/10.1214/11-BA618

Cael, B. B., Cavan, E. L., & Britten, G. L. (2021). Reconciling the size-dependence of marine particle sinking speed. *Geophysical Research Letters*, *48*(5), e2020GL091771. https://doi.org/10.1029/2020GL091771

Chase, Z., & Anderson, R. F. (2004). Comment on "on the importance of opal, carbonate, and lithogenic clays in scavenging and fractionating ^{230}Th, ^{231}Pa and ^{10}Be in the ocean" by S. Luo and T.-L. Ku. *Earth and Planetary Science Letters*, *220*(1–2), 213–222. https://doi.org/10.1016/S0012-821X(04)00028-7

Gottschalk, J., Szidat, S., Michel, E., Mazaud, A., Salazar, G., Battaglia, M., et al. (2018). Radiocarbon measurements of small-size foraminiferal samples with the Mini Carbon Dating System (MICADAS) at the University of Bern: Implications for paleoclimate reconstructions. *Radiocarbon*, *60*(2), 469–491. https://doi.org/10.1017/RDC.2018.3

Heaton, T. J., Köhler, P., Butzin, M., Bard, E., Reimer, R. W., Austin, W. E. N., et al. (2020). Marine20 — The marine radiocarbon age calibration curve (0–55,000 cal BP). *Radiocarbon*, *62*(4), 779–820. https://doi.org/10.1017/RDC.2020.68

Jones, G. A., Johnson, D. A., & Curry, W. B. (1984). High-resolution stratigraphy in late Pleistocene/Holocene sediments of the Vema Channel. *Marine Geology*, *58*(1–2), 59–87. https://doi.org/10.1016/0025-3227(84)90116-6

Luo, S., & Ku, T.-L. (2004b). Reply to Comment on "On the importance of opal, carbonate, and lithogenic clays in scavenging and fractionating ^{230}Th, ^{231}Pa and ^{10}Be in the ocean". *Earth and Planetary Science Letters*, *220*(1–2), 223–229. https://doi.org/10.1016/S0012-821X(04)00029-9

Mahowald, N. M., Albani, S., Kok, J. F., Engelstaeder, S., Scanza, R., Ward, D. S., & Flanner, M. G. (2014). The size distribution of desert dust aerosols and its impact on the Earth system. *Aeolian Research*, *15*, 53–71. https://doi.org/10.1016/j.aeolia.2013.09.002

Max, L., Nürnberg, D., Chiessi, C. M., Lenz, M. M., & Mulitza, S. (2022). Subsurface ocean warming preceded Heinrich Events. *Nature Communications*, *13*(1), 4217. https://doi.org/10.1038/s41467-022-31754-x

Missiaen, L., Waelbroeck, C., Pichat, S., Jaccard, S. L., Eynaud, F., Greenop, R., & Burke, A. (2019). Improving North Atlantic marine core chronologies using ^{230}Th normalization. *Paleoceanography and Paleoclimatology*, *34*(7), 1057–1073. https://doi.org/10.1029/2018PA003444

Roy-Barman, M., Foliot, L., Douville, E., Leblond, N., Gazeau, F., Bressac, M., et al. (2021). Contrasted release of insoluble elements (Fe, Al, rare Earth elements, Th, Pa) after dust deposition in seawater: A tank experiment approach. *Biogeosciences*, *18*(8), 2663–2678. https://doi.org/10.5194/bg-18-2663-2021

Tessin, A. C., & Lund, D. C. (2013). Isotopically depleted carbon in the mid-depth South Atlantic during the last deglaciation. *Paleoceanography*, *28*(2), 296–306. https://doi.org/10.1002/palo.20026

Waelbroeck, C., Lougheed, B. C., Vazquez Riveiros, N., Missiaen, L., Pedro, J., Dokken, T., et al. (2019). Consistently dated Atlantic sediment cores over the last 40 thousand years. *Scientific Data*, *6*(1), 165. https://doi.org/10.1038/s41597-019-0173-8

Wunsch, C. (2006). *Discrete inverse and state estimation problems: With geophysical fluid applications*. Cambridge University Press.